© 2021. Published by The Company of Biologists Ltd | Development (2021) 148, dev197558. doi:10.1242/dev.197558

RESEARCH ARTICLE

PRSS50 is a testis protease responsible for proper sperm tail formation and function

Jason M. Scovell[1,2,3,4,*], Juan C. Bournat[2,*], Adam T. Szafran[2], Minerva Solis[2], Joshua Moore[2], Armando Rivera[1,2,5], Ching H. Chen[2], Jason Zhang[2], Nathan Wilken[2], Abhishek Seth[1,2,5] and Carolina J. Jorgez[1,2,5,‡]

ABSTRACT

Multiple morphological abnormalities of the sperm flagella (MMAF) are a major cause of asthenoteratozoospermia. We have identified protease serine 50 (PRSS50) as having a crucial role in sperm development, because *Prss50*-null mice presented with impaired fertility and sperm tail abnormalities. PRSS50 could also be involved in centrosome function because these mice showed a threefold increase in acephalic sperm (head-tail junction defect), sperm with multiple heads (spermatid division defect) and sperm with multiple tails, including novel two conjoined sperm (complete or partial parts of several flagellum on the same plasma membrane). Our data support that, in the testis, as in tumorigenesis, PRSS50 activates NFκB target genes, such as the centromere protein leucine-rich repeats and WD repeat domain-containing protein 1 (LRWD1), which is required for heterochromatin maintenance. *Prss50*-null testes have increased IκκB, and reduced LRWD1 and histone expression. Low levels of de-repressed histone markers, such as H3K9me3, in the *Prss50*-null mouse testis may cause increases in post-meiosis proteins, such as AKAP4, affecting sperm formation. We provide important insights into the complex mechanisms of sperm development, the importance of testis proteases in fertility and a novel mechanism for MMAF.

KEY WORDS: PRSS50, LRWD1, NFκB, IκB, AKAP4, SEPT12, H3K9me3, Infertility, MMAF, Mitochondria, Centrosome, Midpiece, Sperm tail

INTRODUCTION

One in ten men of reproductive age are infertile (Forti and Krausz, 1998; Sharlip et al., 2002; Datta et al., 2016). Although 25% of infertile men have normal semen quality, the majority of infertile men have semen abnormalities, with asthenozoospermia (impaired motility; 51%) and/or teratozoospermia (impaired morphology; 54%) (Wu et al., 2021). In 2014, a new infertility syndrome was defined as multiple morphological anomalies of the flagella (MMAF) to describe a form of asthenoteratozoospermia with a range of sperm tail defects, including absent, short, bent, coiled or irregular tails, which seriously impair sperm motility (Ben Khelifa et al., 2014). The etiology of MMAF is heterogeneous, with more than 20 genes associated with this syndrome, suggesting the involvement of complex molecular mechanisms (Touré et al., 2020; Wang et al., 2020). Currently, diagnosis of MMAF can require transmission electron microscopy (TEM) evaluation, which is resource prohibitive for many patients and clinical centers. Identifying a broad scope of genes responsible for MMAF could provide a more affordable and effective means to deliver actionable treatment plans to patients with otherwise unexplained asthenoteratozoospermia and infertility.

Sperm formation, maturation, capacitation and binding to the oocyte require the function of serine proteases, and their activation and inhibition must be precise in time and place. Several serine proteases, including protease serine (PRSS) 41, PRSS42, PRSS43 and PRSS44, are activated in primary spermatocytes during the late pachytene stage, demonstrating their role in meiotic progression (Yoneda and Kimura, 2013; Yoneda et al., 2013). Some proteases are essential for mouse fertility, as demonstrated by male knockouts of *Prss37* and *Prss55,* which are infertile due to severe sperm tail and motility defects (Shen et al., 2013; Shang et al., 2018). Low levels of PRSS37 are associated with unexplained male infertility (Liu et al., 2016). *Prss21* is important but not essential, because mice lacking this protease are subfertile; however, *Prss21*-null sperm have decreased motility, angulated and curled tails, fragile necks and dramatically increased susceptibility to decapitation (Netzel-Arnett et al., 2009). Thus, serine proteases can range from being important to vital for sperm tail development and function.

PRSS50, also known as testis-specific protease 50 (TSP50), is a protease with a testis-enriched expression pattern and a unique threonine enzymatic triad (Xu et al., 2004). The fact that testicular PRSS50 expression is similar in humans, mice and rats supports the notion of an evolutionarily conserved function required for fertility (Xu et al., 2004). Analogous to other testis-specific proteases, PRSS50 expression is upregulated in some malignancies, such as colorectal, gastric, cervical and non-small cell lung cancers (Zheng et al., 2011; Liu et al., 2014; Yuan et al., 2015; Cao et al., 2018; Conway et al., 2019). PRSS50 promotes the proliferation, migration and invasion of cancer cells involving NFκB-dependent epithelial-to-mesenchymal transition activation by increasing NFκB signaling upon degradation of IκB (Song et al., 2011; Zhang, 2014; Cao et al., 2018). However, little is known of its physiological significance in spermatogenesis. We hypothesized that PRSS50 is as crucial for sperm tail formation as other proteases are, likely by activating genes via NFκB, as occurs in tumorigenesis.

In the present study, we used CRISPR/Cas9 to genetically engineer the first *Prss50*-null mice, which, consistent with our hypothesis, exhibited severe sperm tail defects and increased testicular IκκB. NFκB is a transcription factor for the leucine-rich

[1]Scott Department of Urology, Baylor College of Medicine, Houston, TX 77030, USA. [2]Center for Reproductive Medicine, Baylor College of Medicine, Houston, TX 77030, USA. [3]Translational Biology and Molecular Medicine, Baylor College of Medicine, Houston, TX 77030, USA. [4]Glickman Urological and Kidney Institute, Cleveland Clinic, Cleveland, OH 44195, USA. [5]Department of Surgery, Texas Children's Hospital, Houston, TX 77030, USA.
*These authors contributed equally to this work

‡Author for correspondence (cj129804@bcm.edu)

C.J.J., 0000-0001-9203-6331

Handling Editor: Haruhiko Koseki
Received 5 October 2020; Accepted 18 March 2021

Development (2021) 148, dev197558. doi:10.1242/dev.197558

repeats and WD repeat domain-containing protein 1 (LRWD1), a testis-specific centrosome protein (Lin et al., 2006; Teng et al., 2010). LRWD1 is also known as origin recognition complex-associated protein (ORCA) and has several identified functions, including binding to histones H3 and H4 to organize heterochromatin structure and silence satellite repeats (Bartke et al., 2010; Shen et al., 2010, 2012; Vermeulen et al., 2010; Chan and Zhang, 2012; Wang et al., 2018). LRWD1, which colocalizes with γ-tubulin, is required for proper microtubule nucleation in the human testicular embryonic carcinoma cell line NT2/D1 (Teng et al., 2010; Wang et al., 2018). Loss of LRWD1 results in significantly decreased H3K9Me3, which is important for testicular heterochromatin organization (Wang et al., 2017) because its accumulation starts early in meiosis and coincides with the repression of escape genes. Over 100 sex-linked male reproduction genes escape from chromosome-wide silencing in order to be activated in the post-meiotic round spermatids (Adams et al., 2018).

Histone marks play an important role in the proper regulation of escape genes and these epigenetic memories persist from meiosis to spermatids (Tan et al., 2011). One escape gene important in sperm formation is *Akap4* (Ernst et al., 2019). Our work establishes a novel testicular PRSS50-NFκB-LRWD1 pathway because we also found that, in the absence of *Prss50*, LRWD1 was downregulated. As a consequence, incorrect centrosome formation occurred and total H3 levels, along with modified H3K9me1, H3K9me3 and H2AXs139P, were reduced. Dysregulation of these mechanisms resulted in an upregulation of proteins primarily expressed during spermiogenesis, such as AKAP4. Absence of PRSS50 led to abnormal sperm tails with mislocalization of organelles, including mitochondria, centrioles, microtubules and annuli. These multiple ultrastructural defects in the *Prss50*-null mice affected sperm tail formation to the detriment of cell motility and, consequently, fertility potential. In summary, our studies on *Prss50* deficiency reveal the pathophysiological impact of PRSS50 on sperm tail formation and its potential role as an important contributor to MMAF.

RESULTS

PRSS50 is expressed in spermatocytes, spermatids and sperm

Using immunohistochemistry (IHC), we characterized the temporal-spatial expression pattern of PRSS50 in the mouse testis (Fig. 1), which showed that spermatogonia do not express the protease during embryonic stages or early postnatal days (Fig. 1A, B). At birth, the mouse testis contains only undifferentiated type A1 spermatogonia. By postnatal day (P) 3, differentiation into more advanced spermatogonial stages begins through a series of mitotic divisions. By P7-10, spermatocytes are observed in the leptotene phase of meiosis. By P12, pachytene spermatocytes are present. Round spermatids (postmeiotic cells) are observed by P20 (Nebel

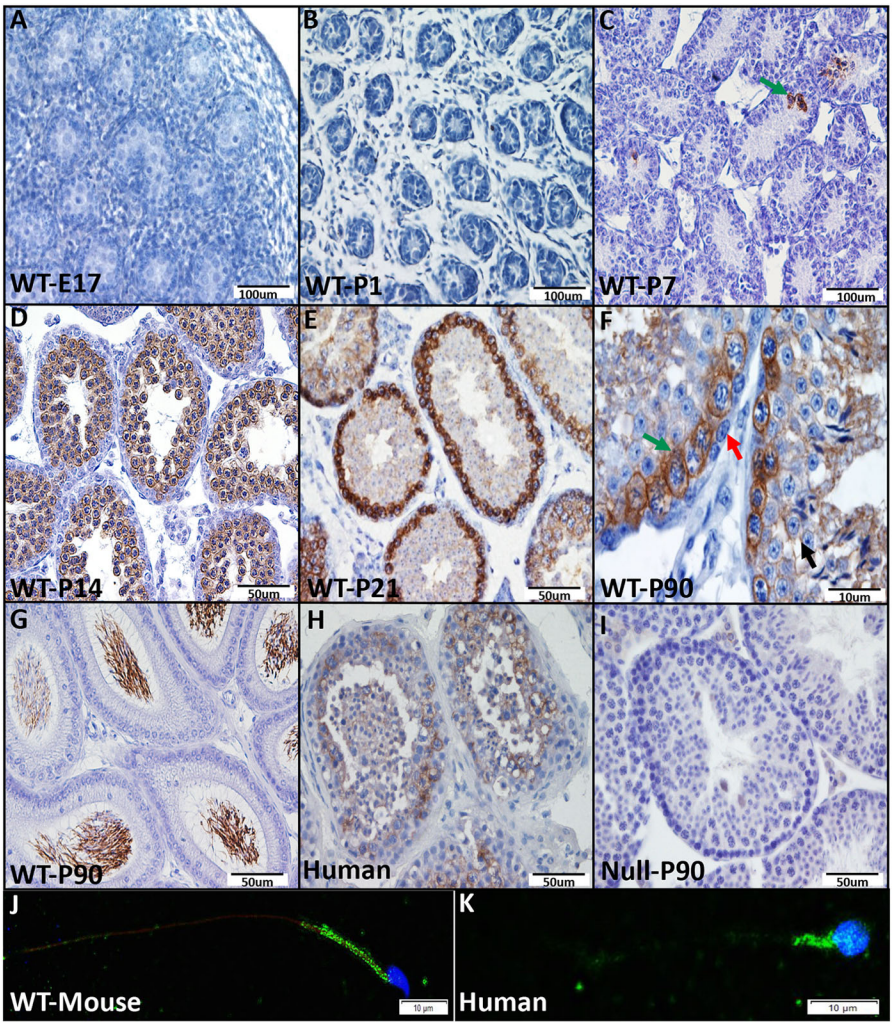

Fig. 1. PRSS50 is expressed in spermatocytes and sperm. (A-I) Light microscopy images of WT mouse and human testes and epididymis stained with a PRSS50 antibody (DAB; brown staining). (A) PRSS50 is not present in mouse embryonic testis at embryonic day (E)17. (B) PRSS50 is not present in mouse P1. (C) PRSS50 expression starts at P7 in leptotene spermatocytes (green arrow). (D,E) PRSS50 is homogenously expressed in spermatocytes in prepubertal mice at P14 (D) and P21 (E). (F) PRSS50 is expressed mainly in the membrane and cytoplasm of spermatocytes in testes of adult mice (green arrow); weak expression is observed in the membrane of spermatids (black arrow) and no expression is observed in spermatogonia (red arrow) or somatic cells of the testis. (G) Epididymal sperm of mice express PRSS50. (H) PRSS50 is expressed in spermatocytes in human testes. (I) *Prss50*-null mice generated using CRISPR/Cas9 technology lacked PRSS50 expression in spermatocytes. (J,K) Sperm expressing PRSS50 (in green) in the midpiece in both WT mouse (J) and human (K). Sperm heads are stained with DAPI. Midpieces in mouse sperm are stained with MitoTracker Deep Red.

Development (2021) 148, dev197558. doi:10.1242/dev.197558

Table 1. Comparison between *Prss50*-null and WT mice at 3 and 7 months of age

Characteristics	WT mice 3 months (*n*=17)	*Prss50*-null mice 3 months (*n*=11)	WT mice 7 months (*n*=21)	*Prss50*-null mice 7 months (*n*=40)
Testis (mg)	103.22±9.85	92.14±12.52	106.69±12.29	105.02±8.06
Epididymis (mg)	43.93±5.62	41.04±5.12	48.66±3.02	46.53±9.63
Sperm motility	**WT mice 3 months *n*=5**	***Prss50*-null mice 3 months *n*=5**		
Total (%)	42.57±0.93	10.5±5.75**		
Progressive (%)	26.00±4.43	4.59±4.59**		
Static (%)	56.79±1.96	89.95±5.76**		
Hyperactivate (%)	3.82±2.20	0.59±0.50**		
Hormones			**WT mice 7 months (*n*=7)**	***Prss50*-null mice 7 months (*n*=6)**
Testosterone (ng/dl)			377.19±457.62	598.86±521.21
FSH (ng/ml)			39.50±10.02	44.00±15.22
LH (ng/ml)			0.67±0.91	1.23±1.62
Fertility			**WT mice 7 months (*n*=8)**	***Prss50*-null mice 7 months (*n*=8)**
Litter after 6 months of mating			5.63±0.74	3.63±1.51**
Time between pregnancies (months)			26.1±2.69	43.68±21.93*
Pups per litter			7.99±2.58	4.54±1.32*
Total pups			379	124

*P<0.01; **P<0.001.

et al., 1961; McCarrey, 2013). PRSS50 expression presented in spermatocytes at P7 and later strongly localized to the cytoplasm of all spermatocytes, continuing throughout adulthood (Fig. 1C-F). Low expression was also present in round and elongated spermatids (Fig. 1F). High PRSS50 expression was detected in epididymal sperm (Fig. 1G), and further localized to the murine sperm midpiece (Fig. 1J). Using human testicular and sperm ejaculate samples, we determined that the PRSS50 expression pattern in human sperm was similar to that in mouse sperm (Fig. 1H,K).

Prss50-null mice have severe fertility defects

Prss50-null mice were generated using CRISPR/Cas9 (Fig. S1A). Guides flanking exon 2 were injected with Cas9 protein into mouse embryos to generate a *Prss50* premature stop codon. We validated PRSS50 protein loss in the testis of *Prss50*-null mice by IHC and western blot (Fig. 1I and Fig. S1B). We compared testicular and epididymal weights of wild-type (WT) and *Prss50*-null mice at 3 and 7 months. There was no difference in testicular or epididymal weights between the two groups (Table 1). We performed computer-assisted sperm analysis (CASA), which demonstrated that, compared with WT control mice (Movie 1), *Prss50*-null mice had a significant decrease in sperm motility (Table 1), as shown in Movies 2-5. We assessed fertility by natural mating of *Prss50*-null males to WT females. Of the ten *Prss50*-null males studied, 20% (n=2) were infertile, compared with 0% of WT males (n=8). The remaining 80% of *Prss50*-null males (n=8) were severely subfertile, producing fewer litters and fewer numbers of pups per litter (Table 1, Fig. 2A,B, P<0.01). At the end of the mating period, *Prss50*-null mice produced 40% fewer litters and 67% fewer pups compared with WT mice. We performed hormonal analysis of testosterone, FSH and LH in six *Prss50*-null mice, with no significant differences observed compared with WT mice (Table 1).

Prss50-null mice show abnormal testicular and epididymal morphology

To understand the cause of reduced fertility in *Prss50*-null mice, we evaluated testicular and epididymal histology (Fig. 3). *Prss50*-null mice had normal testicular weight at any age (Table 1). Although most seminiferous tubules (STs) in *Prss50*-null mice contained germ cells, there were many spermatogenic abnormalities in the STs, including: STs missing several types of germ cell and, in some cases, lacking all germ cells [Sertoli cell-only (SCO) tubules]; STs with a high degree of vacuolation; STs with multinucleated and symplastic spermatids; and STs with increased residual bodies (Fig. 3B-G). We additionally found increased residual bodies in the epididymis (Fig. 3H). To verify whether the germ cells were

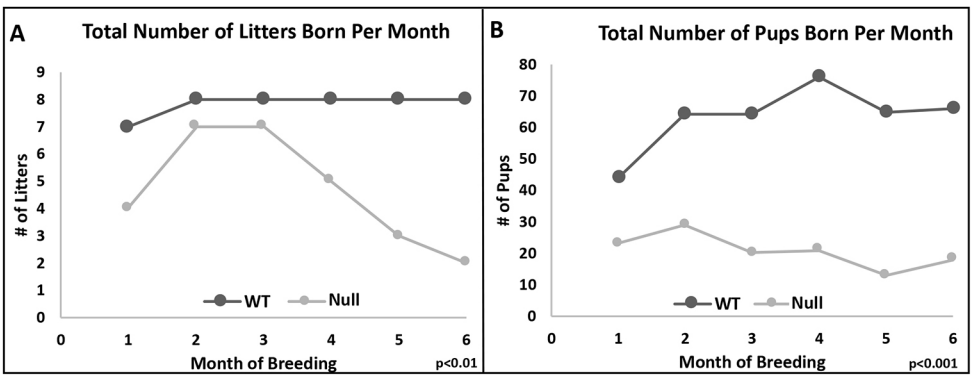

Fig. 2. *Prss50*-null mice have impaired fertility. (A) Comparison of the total number of litters per month produced by equal numbers of WT and *Prss50*-null mice in a 6-month mating period; P<0.01. (B) Comparison of the total number of pups produced per month by equal numbers of WT and *Prss50*-null mice in a 6-month mating period; P<0.001. n=10; however, eight mice per group are represented in the graphs because two *Prss50*-null mice were infertile.

Development (2021) 148, dev197558. doi:10.1242/dev.197558

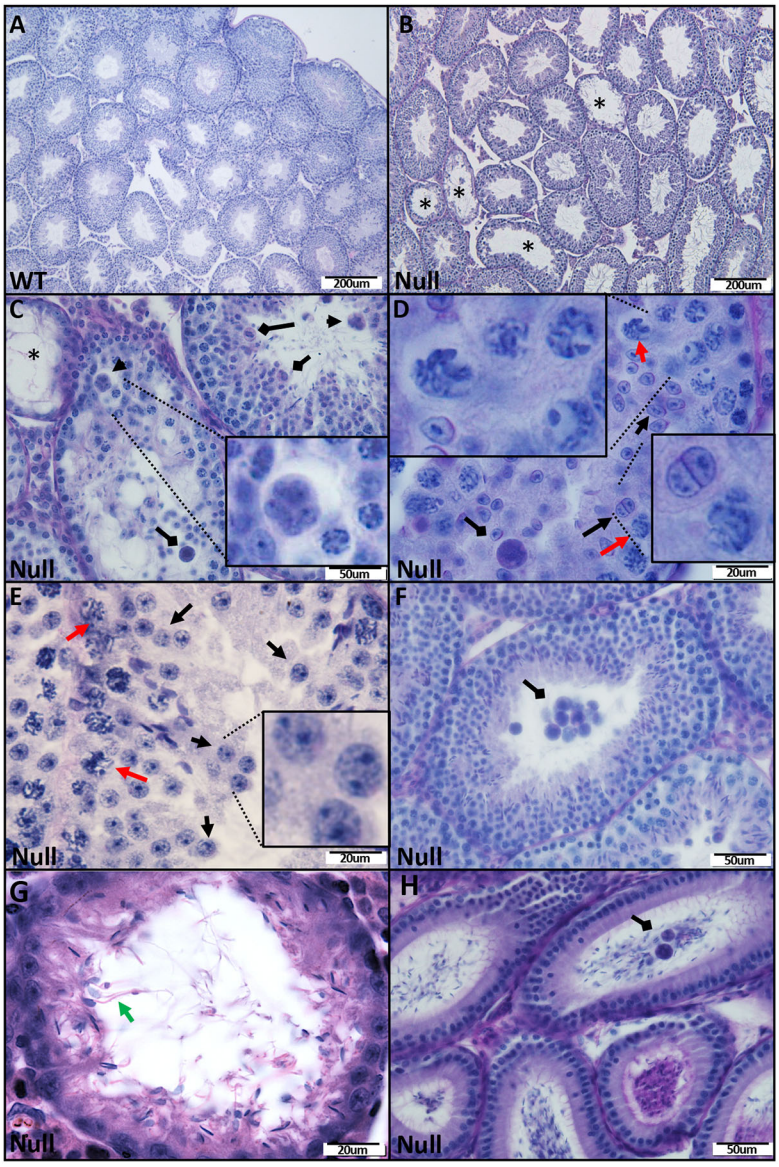

Fig. 3. *Prss50*-null mice have abnormalities in seminiferous tubules and epididymis. (A) WT mice showing normal germ cell layer distribution, with the least mature cells near the basal layer and the most mature cells near the lumen of the STs. (B-G) Testes of *Prss50*-null mice showing different ST abnormalities. (B) Testes of *Prss50*-null mice showing a mix of normal STs and other STs depleted of some or all layers of germ cells (asterisks). (C) *Prss50*-null mice have SCO STs (asterisk), symplasts (arrowheads), vacuoles and residual bodies (rhomboids). (D-F) STs with residual bodies and multinucleated cells (black arrows), and spermatocytes with abnormalities in the paired homologous chromosomes (red arrows). Rhomboids show residual bodies. (G) STs with elongated spermatids at different stages and possible double-headed sperm (green arrow). (H) *Prss50*-null mice have residual bodies (rhomboid) in the epididymis. Testis and epididymis 5 µm paraffin sections were stained with PAS. Scale bars: 200 µm in A,B; 50 µm in C,F,H; 20 µm in D,E,G.

affected, we evaluated the testes using IHC against PLZF (Zbtb16), CCND1 and Ki67 (Mki67), and confirmed that there were no apparent differences (Figs S2C-E and S3). In addition, there was no difference in the presence of somatic cells (i.e. Sertoli and Leydig cells) after evaluation with antibody probes specific to 3β-HSD (Hsd3b6), AR and SOX9 (Figs S2A,B and S3). Moreover, no changes in the formation of intracellular bridges assessed by TEX14 staining were noticed (Figs S2F and S3).

Spermatids of *Prss50*-null mice have impaired cell division, increased phagocytic vesicles and centriole defects associated with abnormal sperm formation

To further characterize the underlying mechanisms driving altered sperm morphology identified by light microscopy, we performed ultrastructural analysis by TEM on testicular and epididymal sperm (Fig. 4). Spermatids from *Prss50*-null mice demonstrated multiple acrosomal caps inside a common cytoplasm without membranes dividing the nucleus, suggesting impaired cell division (Fig. 4B-D); there was also an increase in vesicle formation as tails begin to organize (Fig. 4K,N). These defects in cell division produced sperm with multiple heads and tails (Fig. 4H). *Prss50*-null mice had multiple axonemes in the plasma membrane with swollen mitochondria and organelle disorganization (Fig. 4F-H). The presence of multiple axonemes per plasma membrane produced sperm with multiples tails in the same plasma membrane (Fig. 4R). There was also an abnormal connection between the proximal centriole and nucleus in sperm from *Prss50*-null mice, and elongated spermatids lacking centrioles or having multiple centrioles were consistently identified (Fig. 4G,H,J,K,N,P,R-T), which could cause a defect in the anchoring of the head to the sperm neck.

Sperm from *Prss50*-null mice have abnormal morphology

To assess the consequences of the abnormal testicular and epididymal histology identified in *Prss50*-null mice, we evaluated sperm morphology. To minimize bias, we developed a High Content Analysis (HCA) automated image-based analysis platform to quantify sperm morphology (Fig. 5 and Fig. S4), in which sperm from WT and *Prss50*-null mice were processed simultaneously to minimize technical variation. We found that, compared with WT controls, *Prss50*-null mice had a decreased percentage of normal

Development (2021) 148, dev197558. doi:10.1242/dev.197558

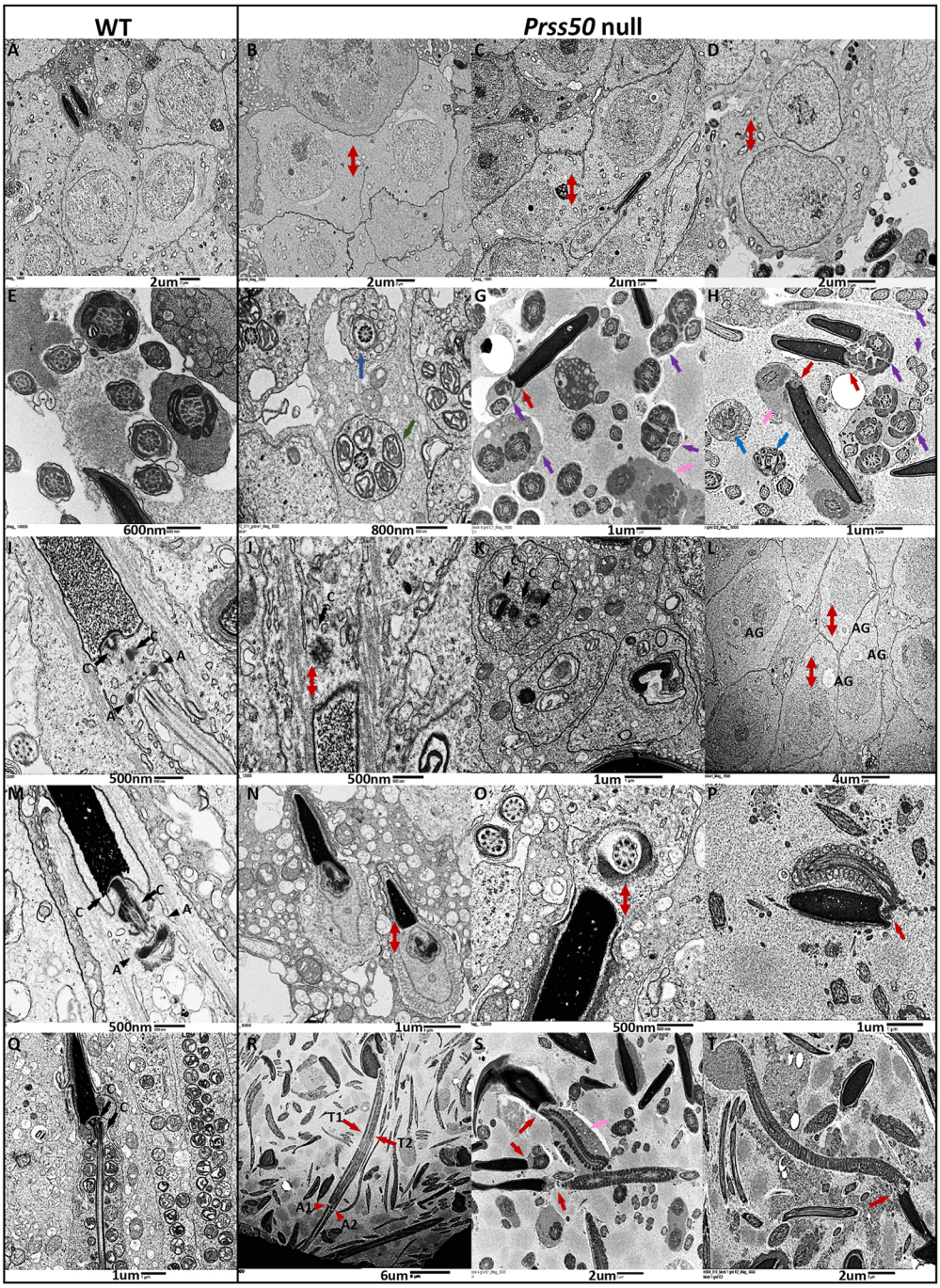

Fig. 4. *Prss50*-null mouse testes and epididymis have ultrastructural abnormalities. (A-T) TEM images of mouse testes (A-D,L) and epididymis (E-K,M-T). (A) WT mouse showing two spermatids in the cap phase of acrosomal biogenesis with well-delineated cell membranes. (B-D) *Prss50*-null mice showing two spermatids in the cap phase with different degrees of membrane separation between cells (red double-headed arrows). (E) WT mouse showing different segments of sperm flagellum and cross-section of the midpiece, revealing the regular arrangement of mitochondria, outer dense fibers and microtubules with a '9+2' arrangement and one axoneme per plasma membrane. (F) Cross-section of *Prss50*-null mouse midpiece showing a microtubule '9+2' arrangement but swollen and disorganized mitochondria (green arrow), and abnormal tail organization (blue arrow). (G,H) *Prss50*-null mouse showing numerous axonemes (purple arrows) in the same plasma membrane and sperm head often associated with a mass of cytoplasm where components of flagellum were found but could not be assembled correctly at the tail (pink arrows). Red arrow in G shows abnormal head-neck connection. (H) *Prss50*-null sperm with two heads and two axonemes in the same plasma membrane. Red arrow shows abnormal head-neck connection and blue arrows show abnormal cross section of sperm flagellum. (I,M) Elongated spermatid in WT mice showing a proximal centriole (C) well attached to the nuclear membrane and a distal centriole and annuli (A) on each side of the beginning of the tail. (J,N-P,S,T) In most of the *Prss50*-null sperm, the centriole does not appear to be properly attached to the nuclear member or is attached offsite (red double-headed arrows), the axonemes have abnormalities and there are abundant vesicles. Red arrows in P,S,T show abnormal head-neck connection. Pink arrow in T shows excess of residual cytoplasm with accumulation of many organelles including mislocalized mitochondria. (K) *Prss50*-null mice with additional centrioles. (L) *Prss50*-null sperm with acrosomal granules (AG) not properly attached to the nuclear membrane. (P) *Prss50*-null sperm with a short tail (red arrow). (Q) WT sperm with the centriole (C) attached to the head and a single tail surrounded by dense mitochondria. (R) *Prss50*-null sperm with one head and two tails (T1 and T2) running in parallel in the same plasma membrane and two sets of annuli (A1 and A2). Scale bars: 6 µm in R; 4 µm in L; 2 µm in A-D,S,T; 1 µm in G,H,K,N,P,Q; 800 nm in F; 600 nm in E; 500 nm in I,J,M,O.

Development (2021) 148, dev197558. doi:10.1242/dev.197558

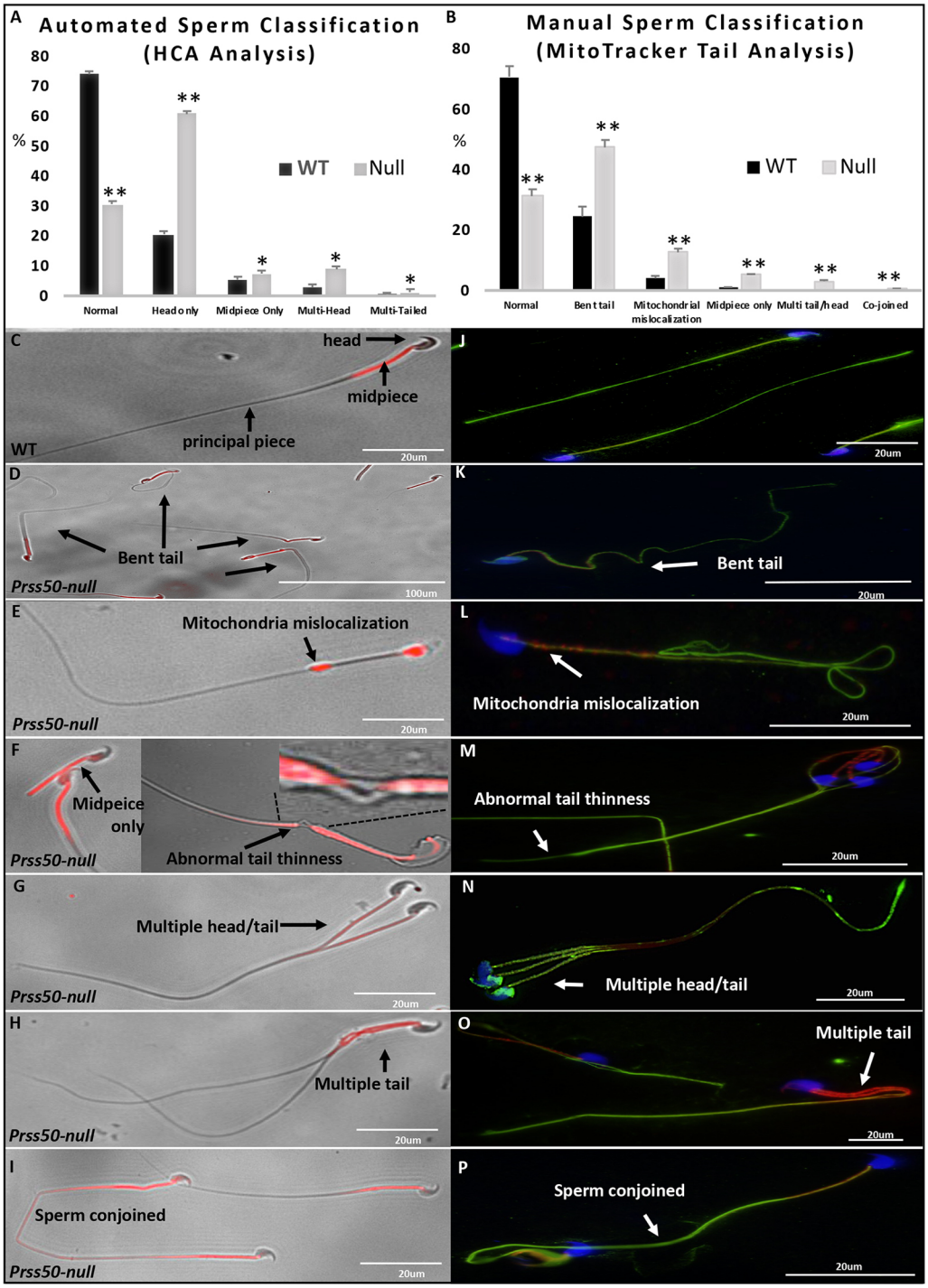

Fig. 5. *Prss50*-null mice have significant sperm abnormalities. (A) Sperm from WT and *Prss50*-null mice labeled with DAPI (head), MitoTracker Deep Red (midpiece) and α-tubulin (tail) were subjected to HCA analysis. Sperm were classified as normal (one head attached to one tail and no apparent defect in midpiece); head only (head without tail attached); midpiece only (sperm that have an identified head, a MitoTracker Deep Red-positive midpiece, but no or a minimal α-tubulin-stained tail extending beyond the midpiece); multi-head (sperm with multiple heads attached); and multi-tailed (more than two tails attached to a head). In total, 10,000 sperm from each sample (n=5) were classified using a rule-based scheme. Graphs show the percentage of total sperm. Data are mean±s.e.m. *P<0.01; **P<0.001. (B) Manual sperm classification of sperm in which the head and midpiece (labeled with MitoTracker Deep Red) were attached. In total, 200 sperm per sample (n=20) were counted on bright-field under a 40× objective. Graphs show the percentage of total sperm. Data are mean±s.d. Sperm were classified and examples of each classification are indicated as: (C) normal sperm with one head attached to a single tail (tail midpiece labeled red followed by unlabeled principal piece); (D) bent-tail sperm, in which the tail forms an angle; (E) mitochondria-mislocalization sperm in which MitoTracker Deep Red is either observed in multiple areas of the tail or is absent; (F) midpiece-only sperm, in which only the midpiece is observed but not the principal piece, probably because of a decrease in midpiece thickness and number of mitochondria, which could cause sperm tail breaks; (G) multiple tails/heads: a sperm sharing multiple midpieces and heads; (H) sperm with a single head and multiple tails; (I) conjoined sperm – with two sperm heads conjoined by a single tail. (J-P) Sperm labeled with DAPI (head), α-tubulin (tail) and MitoTracker Deep Red (midpiece). (J) WT sperm with normal tail morphology. (K-P) *Prss50*-null sperm with different tail anomalies. Scale bars: 100 µm in D; 20 µm in J-P.

Development (2021) 148, dev197558. doi:10.1242/dev.197558

sperm (Fig. 5A, 30% versus 72%, $P<0.01$), and we identified a threefold increase (61% versus 21%, $P<0.01$) in the number of sperm heads without a tail attached, suggesting a fragile connection between sperm head and tail that causes acephalic sperm. Interestingly, *Prss50*-null sperm had increased numbers of multiple heads and multiple tails.

We validated the HCA data by manual sperm morphological analysis of intact sperm (Fig. 5B) and labeled sperm with MitoTracker Deep Red to allow mitochondrial localization to the midpiece (Fig. 5B-I and Fig. S5). To further visualization of the defects, the sperm were stained with α-tubulin to allow better visualization of the tail (Fig. 5J-P). By manual analysis, we were able to characterize the tail morphology more accurately into several categories: (1) bent tails; (2) abnormal mitochondrial location (gaps in MitoTracker Deep Red); (3) midpiece only (head+midpiece only); (4) multiple tails that, in some cases, also include multiple heads; and (5) conjoined sperm (Fig. 5B-I and Fig. S5). All categories of *Prss50*-null and WT sperm were significantly different from each other. Of note, we did not observe any conjoined sperm or sperm with multiple tails or heads in any of the 20 WT (n=4000 sperm) mice analyzed, indicating that the appearance of abnormal morphologies is not common during spermatogenesis. The conjoined and multiple tail sperms were able to move only statically, as indicated in Movies 2-4. Other sperm, such as those with two heads, demonstrated progressive motility (Movie 5). No abnormalities in head morphology were observed. Furthermore, after performing HCA sperm chromatin structure assays (HCA-SCSAs), no differences in DNA damage between WT and Prss50-null sperm were detected (Fig. S6).

Mislocalized mitochondria, microtubule and annulus proteins in *Prss50*-null sperm

Given our observation of mitochondria and annulus mislocalization by TEM, we sought to validate these findings in sperm using super-resolution microscopy. We labeled mitochondria with MitoTracker Deep Red and performed immunofluorescence (IF) against septin 12 (SEPT12), an annulus-specific protein, and α-tubulin, an important protein in tail structure and organelle organization. Whereas mitochondria in WT sperm specifically localized along the midpiece with distinct discontinuation at the annulus (Fig. 6A), the organelle organization in the *Prss50*-null sperm was disrupted with varying levels of mitochondrial absence throughout the midpiece (Fig. 6E,F) and aggregate formation (Fig. 6B,E). Moreover, α-tubulin was uniformly distributed throughout the tail in WT sperm (Fig. 6D) but not in *Prss50*-null sperm, with disorganization in α-tubulin expression present in both the midpiece and principal piece (Fig. 6E,F). Interestingly, areas of low α-tubulin and Mitotracker Deep Red often colocalized, suggesting disrupted microtubule organization as a mechanism for mislocalized organelles within the *Prss50*-null sperm tail (Fig. 6F).

The sperm annulus is a septin-based fibrous ring structure that starts developing during early spermiogenesis, encircling the axoneme at the distal end of the basal body. As the sperm flagellum develops, the annulus slips towards a more distal position,

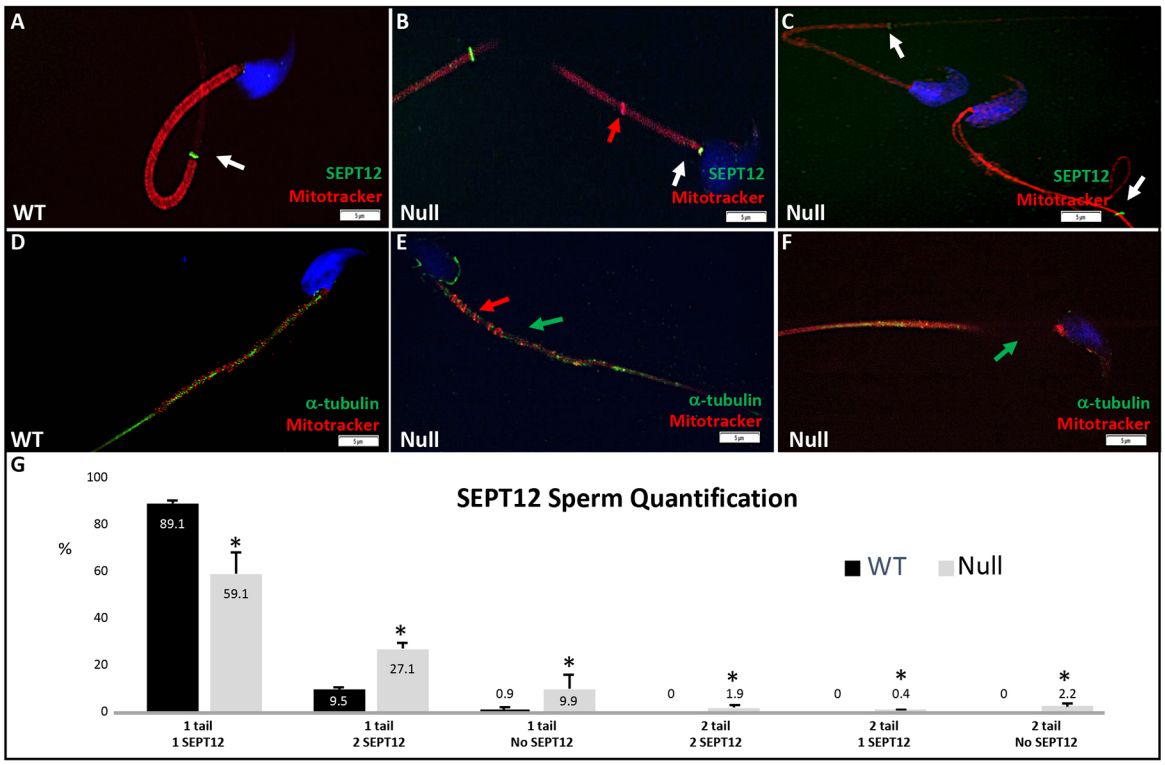

Fig. 6. *Prss50*-null sperm have annulus and tail abnormalities. (A) WT sperm express SEPT12 (green, white arrow) in the annulus at the distal end of the midpiece; mitochondria in the midpiece are labeled with MitoTracker Deep Red and the head is labeled with DAPI (blue). (B,C) *Prss50*-null sperm have normal SEPT12 localization (white arrows). Red arrow indicates abnormal mitochondria accumulation. (D) WT sperm express α-tubulin (green) along the tail. (E,F) *Prss50*-null sperm have a disrupted α-tubulin pattern, especially in the midpiece (red), indicated by green arrows. Red arrows indicate abnormal mitochondria accumulation. (G) *Prss50*-null mice have a significant decrease in sperm number, with a single SEPT12 signal in the annulus at the end of the midpiece and a significant increase in sperm either lacking SEPT12 signal or having an extra SEPT12 signal. Graphs show the percentage of total sperm. Data are mean±s.d.*$P<0.01$.

Development (2021) 148, dev197558. doi:10.1242/dev.197558

and the mitochondria begin to affix to the flagellum. In the mature sperm, the annulus connects the midpiece and the principal piece of the flagellum (Kuo et al., 2015; Shen et al., 2017), whereas SEPT12 organizes the septin filaments at the sperm annulus. The annulus is a crucial component required for proper sperm function and, hence, most sperm cells in WT mice express SEPT12 only at the connection of the midpiece and principal piece (Fig. 6A). On the other hand, although most *Prss50*-null sperm with one head had a standard annulus location (59%; Fig. 6C), it was common to find sperm with two SEPT12 signals (27%), with the additional SEPT12 signal retained immediately below the connecting piece, indicating a defect of the annulus migration caudally (Fig. 6B), and sperm with no SEPT12 signal (10%; Fig. 6C). Sperm with multiple tails often lacked the SEPT12 signal in one of the tails (Fig. 6C). We did not commonly identify these abnormalities in WT sperm (Fig. 6G).

Given that the mitochondrial organization was abnormal, we investigated whether the mitochondrial membrane potential was impaired. We developed an additional HCA algorithm to identify active mitochondria along with normal versus abnormal mitochondrial distribution patterns based on JC-1 (a red/green-shift mitochondrial membrane potential-sensitive dye) staining (Fig. 7). We found that, compared with WT controls, an increase in the total JC-1 red signal in *Prss50*-null sperm was readily detected (Fig. 7A; 1.56±0.12 versus 1.0±0.01; $P<0.01$). This increased signal was not associated with a significant difference in the red-to-green ratio (2.0 versus 1.7) and was sensitive to the inhibitor of oxidative phosphorylation, carbonyl cyanide m-chlorophenyl hydrazone (CCCP). Sperm from *Prss50*-null mice tended to have a significantly smaller total active mitochondrial area per sperm (Fig. 7B; 806±12 versus 1146±27 pixels; $P<0.01$) and a greater frequency of the truncated 'abnormal' phenotype compared with sperm from WT mice (Fig. 7C,D; 65.3±0.3 versus 10.2±0.4: $P<0.001$). The area of active mitochondria was reduced in *Prss50*-null sperm, correlating to aggregates previously observed by fluorescence, but the fact that overall membrane potential was normal suggests that mitochondrial function is not impaired.

Prss50 knockout disrupts normal testis PRSS50-IkB-LRWD1-histone signaling

PRSS50 has been shown to promote cell proliferation via the activation of NFκB signaling, which enhances the expression of NFκB target genes. In the absence of PRSS50, IκB increases and NFκB activation decreases because of the increase in its inhibitor (Song et al., 2011; Zhang, 2014). PRSS50 interacts directly with the NFκB:IκB complex, as demonstrated by PRSS50-T310A mutation, which blocks the interaction with the NFκB:IkBa complex and the ability of PRSS50 to promote cell proliferation (Yuan et al., 2015). The level of IκκB, one of the two subunits of IκB, was measured and demonstrated an eightfold increase in *Prss50*-null testis (Fig. 8B). The increased inhibition of the NFκB pathway could affect NFκB target gene activation. One of the targets of NFκB in the testis is the centrosome protein LRWD1 (Teng et al., 2012). LRWD1 is expressed in the cytoplasm of spermatocytes and spermatids and in the head-neck connection of the sperm (Teng et al., 2010). We determined the testicular levels of LRWD1 and found a 2.1-fold decrease in *Prss50*-null mice compared with WT controls (Fig. 8A). Given that NFκB positively regulates LRWD1 promoter activity (Teng et al., 2012), the decrease in LRWD1 could be because of the failed activation of NFκB signaling.

LRWD1 is important for heterochromatin formation and microtubule nucleation from centrioles. LRWD1, a subunit of the origin recognition complex (ORC), is a methylation-sensitive nucleosome interactor involved in both initiation of DNA replication and heterochromatin silencing (Bartke et al., 2010). Interestingly, LRWD1 preferentially binds to trimethylated repressive histone marks, especially H3K9me3 (Chan and Zhang, 2012); therefore, our observation that H3K9me3 protein was absent in *Prss50*-null testis is noteworthy (Fig. 9E). IF using H3K9me3 antibodies indicated a decrease in testicular H3K9me3, especially in round spermatids (Fig. 9N-P). To confirm the absence of H3K9me3, we performed a western blot with ten times more

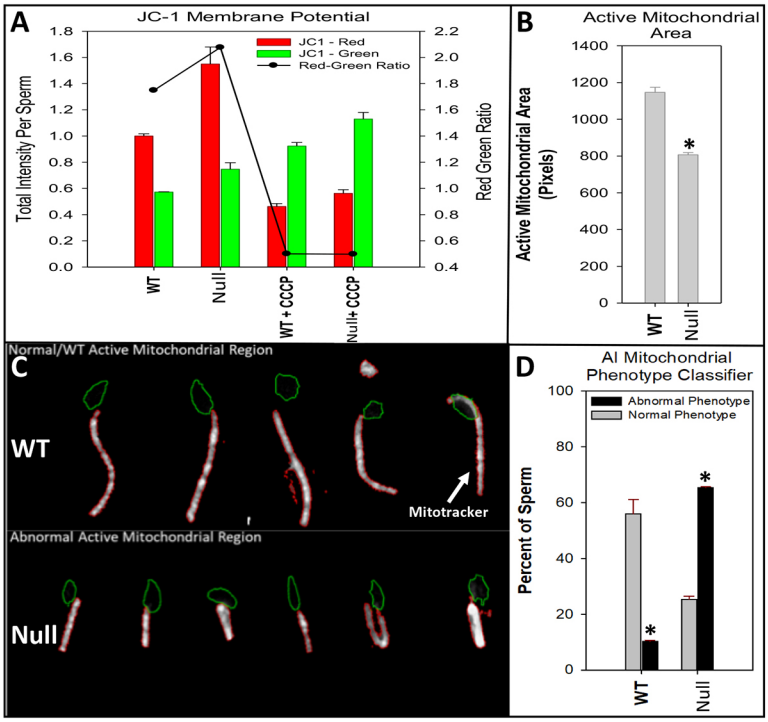

Fig. 7. Sperm from *Prss50*-null mice have a smaller total active mitochondrial area per sperm compared with WT sperm. HCA was used to quantify effects of PRSS50 deficiency on membrane potential of active mitochondria labeled using JC-1, a green-red dye sensitive to mitochondrial membrane potential. HCA combines the use of automated microscopy and image analysis algorithms to image, segment and measure thousands of individual sperm per sample. (A) There was an increase in total JC-1 (red signal) per sperm (1.56±0.12 versus 1.0±0.01; $P<0.01$) from *Prss50*-null mice compared with wild type. This increased signal was not associated with a significant difference in the red-to-green ratio (2.0 versus 1.7) and was sensitive to the mitochondrial poison CCCP. (B) Sperm from *Prss50*-null mice had a smaller total active mitochondrial area per sperm (806±12 versus 1146±27 pixels; $P<0.01$). (C) Manual inspection of the images demonstrated two predominant mitochondrial morphology patterns (white areas indicate mitochondria) that differed between WT and *Prss50*-null sperm. (D) To determine the frequency of each pattern in the sperm samples, a cross-validated random forest artificial intelligence model was trained with 200 examples of each pattern. After two rounds of training, the model achieved a ROC AUC greater than 0.9, indicating a high degree of accuracy. When the model was applied to the sperm samples, *Prss50*-null mice had a significantly higher frequency of the truncated 'abnormal' phenotype than did WT mice (65.3±0.3 versus 10.2±0.4; $P<0.001$; data are average±s.e.).

Development (2021) 148, dev197558. doi:10.1242/dev.197558

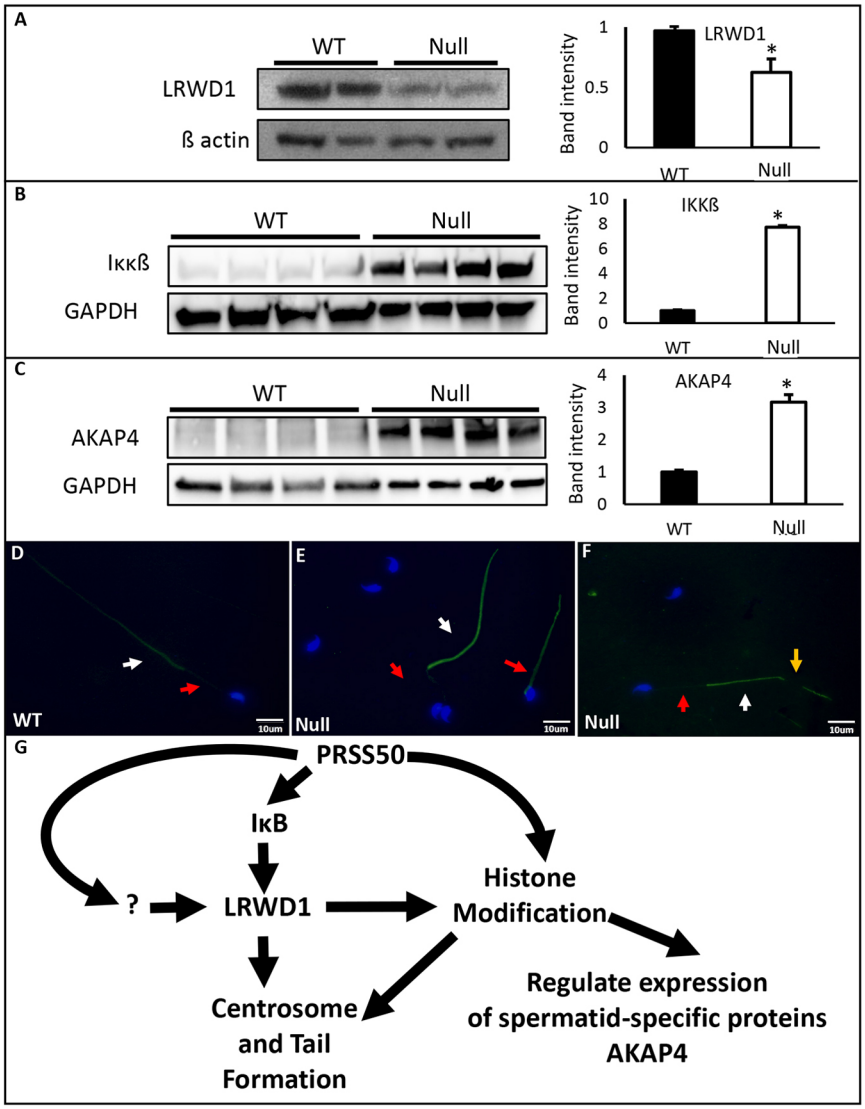

Fig. 8. *Prss50*-null mice have decreased testicular LRWD1 and increased IκκB and spermatid-specific proteins, such as AKAP4. (A) Western blot indicating a 40% downregulation in testicular LRWD1 levels in *Prss50*-null mice versus WT mice. Western blots indicating that (B) testicular IκκB was upregulated eightfold and (C) testicular AKAP4 was upregulated fourfold in *Prss50*-null mice. Graphs in A-C show band intensities. Data are average±s.d. **P*>0.01. (D) AKAP4 expression (green) in WT sperm only in the principal piece (white arrow); the midpiece (red arrow) lacked AKAP4 expression; head was stained with DAPI. (E) AKAP4 expression (green) only in the principal piece (white arrow) of a *Prss50*-null sperm with two heads and in the principal piece (green) and midpiece (green; red arrow) of a single-headed *Prss50*-null sperm. (F) Discontinuous AKAP4 expression in the principal piece (yellow arrow) of a *Prss50*-null sperm. Red and white arrows indicate midpiece and principal piece, respectively. (G) Proposed model indicating the mechanism by which PRSS50 acts in the testis through multiple pathways, including degradation of the IκB pathway to regulate the expression of NFκB target genes, such as *LRWD1*. LRWD1 plays an important role in centrosome and tail formation as well as histone post-translational modifications, which are important for the temporal-spatial activation of spermatid-specific proteins, such as AKAP4. '?' indicates a possible but unidentified protein.

protein in the *Prss50*-null than in the WT mice, which demonstrated similar levels in both groups, to emphasize a decrease by at least ten times in H3K9me3 (Fig. 9J).

The levels of total H3 (H3.1, H3.2, H3.3 and CENP-A) and H3.3, and of the modified histones H3K9me1 and H2AXS139P were determined to identify whether the decrease in histone was specific to H3K9me3. All tested histone markers were significantly reduced (Fig. 9A-D), with H3K9me1 and H2AXS139P being the least affected. We confirmed that these histones were not absent by using ten times more protein from *Prss50*-null testis (Fig. 9F-I). In spermatocytes, H3K9me3 plays an important role by repressing spermatid-specific genes strongly, one of which is *Akap4,* a well-known X-linked escape gene (Ernst et al., 2019). AKAP4 protein levels were increased 3.5-fold in *Prss50*-null testis, indicating that the regulation of spermatid proteins, such as AKAP4, is lost (Fig. 8C). In the testis, AKAP4 is expressed in the appropriated cell type with no apparent difference (Fig. S7). However, in the sperm, although most of the *Prss50*-null sperm had AKAP4 expression in the expected location (the principal piece), there were *Prss50*-null sperm with expression in the midpiece or with discontinuous AKAP4 expression in the principal piece, correlating with abnormal tail formation (Fig. 8D-F).

DISCUSSION

We characterized the temporal-spatial patterns of PRSS50 within the testis and found that expression coincides with the beginning of meiosis as early as leptotene in spermatocytes at P7. This finding is supported by recent data that identified PRSS50 as a major marker of spermatocytes in the leptotene phase (Ernst et al., 2019). Although it is possible that *Prss50* is expressed in somatic cells, our data and data from others indicate that it is unlikely. Low expression, if found in Sertoli cells, may represent protein recycling because of the role of Sertoli cells in the removal of apoptotic germ cells (Ernst et al., 2019). Based on these findings, we hypothesized that PRSS50 contributes to sperm development and possibly fertility. We generated *Prss50*-null mice, which confirmed aberrant sperm morphology and displayed impaired fertility. *Prss50*-null mice had normal testicular size, and all germ cell types and somatic cells were present. However, testicular histology suggested incomplete cell division, as evidenced by an increase in residual bodies and multinucleated and symplastic germ cells. Failures in meiotic cytokinesis result in signature defects, including multinucleated spermatids (O'Donnell et al., 2012; O'Donnell, 2014). The presence of multinucleated spermatids could suggest meiotic defects impairing spermatid development. These giant spermatid

Development (2021) 148, dev197558. doi:10.1242/dev.197558

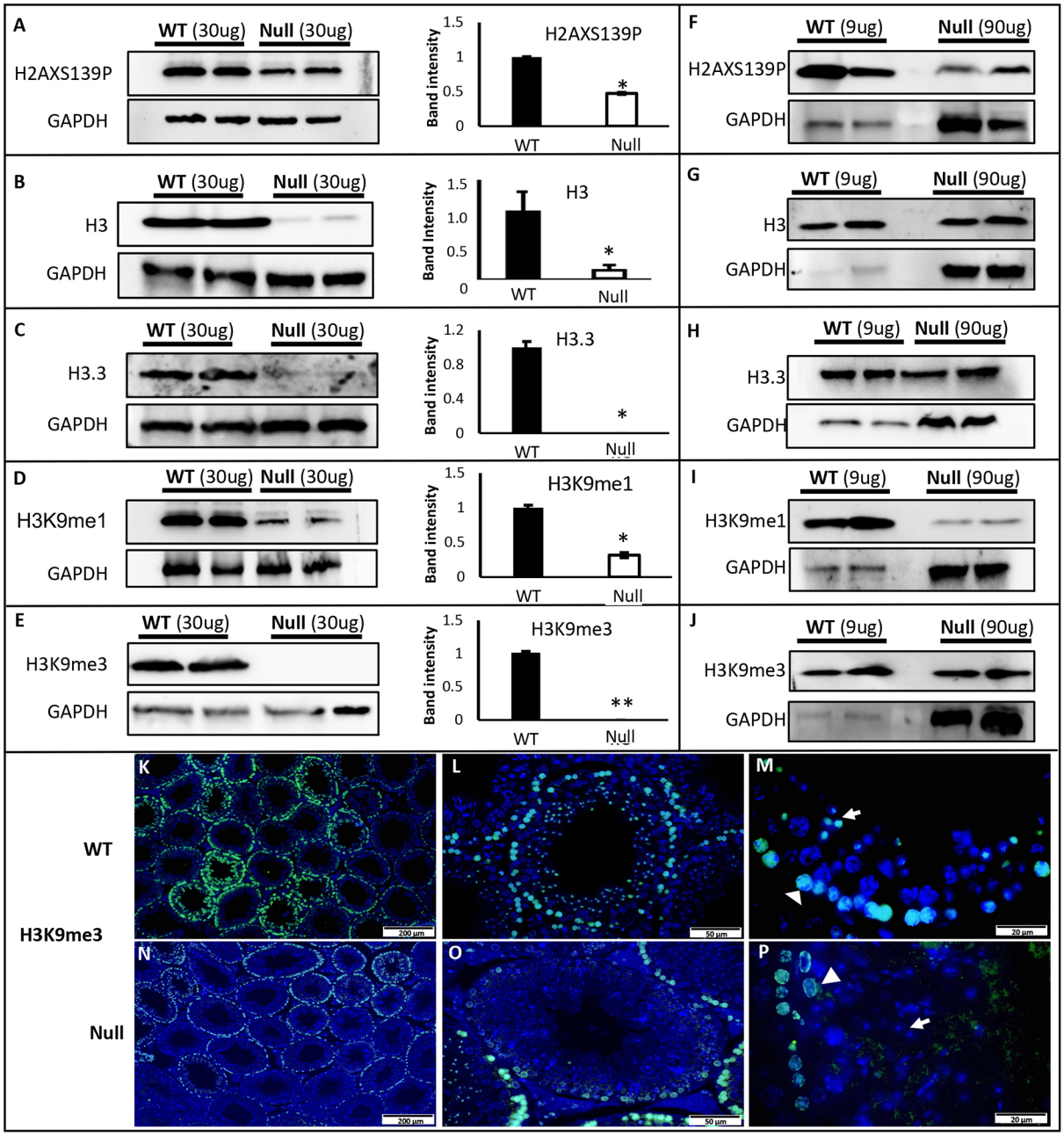

Fig. 9. *Prss50*-null mice have decreased total histone protein expression and post-translational modification. (A-E) Western blots for different histones and their post-translation modification(s) normalized to GAPDH and quantified using ImageJ. Graphs show western blot band intensities. Data are average±s.d. **P*>0.01; ***P*>0.001. (A) H2AXS139P was 50% downregulated. (B) Total H3 (H3.1, H3.2, H3.3 and CENP-A) was 75% downregulated. (C) Testis-specific H3.3 was 90% downregulated. (D) H3K9me1 was 60% downregulated. (E) H3K9me3 was 100% downregulated. (F-J) Ten times more testis-null protein (90 µg) was added than to wild type (9 µg) to demonstrate that the histone proteins were produced but in reduced levels. (K-M) WT mice express H3K9me3 (green) in the nucleus (DAPI-blue) of spermatocytes (arrowhead) and spermatids (white arrow). (N-P) *Prss50*-null mice have decreased levels of H3K9me3, especially in the spermatids (white arrow), and abnormal localization in spermatocytes (arrowhead). Scale bars: 200 µm in K,N; 50 µm in L,O; 20 µm in M,P.

cells with multiple nuclei occur as a result of the widening of narrow intercellular bridges that normally connect spermatogenic epithelial cells (Morton et al., 1986). Through the use of TEM, we were able to identify failed cytokinesis resulting from *Prss50* loss. Meiosis II and cytokinesis in male germ cells are not well understood, because mouse models of meiotic gene defects arrest in the early stages of meiosis, and production of mature sperm does not occur (Kimmins et al., 2007; Jordan et al., 2012; Clement et al., 2015; Gopinathan et al., 2017). Multinucleated spermatids in the testis of *Prss50*-null mice suggest a role for PRSS50 during meiosis.

MMAF is differentiated from other forms of asthenoteratozoospermia by the following: the annulus does not properly migrate ventrally and, although mitochondria can be mislocalized, they are functionally active (Wang et al., 2020). PRSS50 expression in the midpiece suggests a role in midpiece organization, proper annulus formation, mitochondria organization and the pathology of MMAF. This role is supported further by the disorganization of organelles and structures within the *Prss50*-null sperm tail, including abnormally positioned mitochondria but with normal membrane potential and mislocalized annuli. SEPT12

Development (2021) 148, dev197558. doi:10.1242/dev.197558

phosphorylation has been shown to cause annulus disruption, resulting in disassociation from other septin complexes (Shen et al., 2017). Additional signs of improper annulus formation in *Prss50*-null sperm include mitochondrial thinness and bent tails (Shen et al., 2017). Previous studies have shown that there is a correlation between SEPT12 expression and α- and b-tubulin assembly (Kuo et al., 2013). We speculate that disorganized α-tubulin assembly is a contributing factor to the sperm tail phenotype in *Prss50*-null mice.

No defects in the *Prss50*-null HCA-SCSAs were identified, suggesting that the lack of PRSS50 mainly affects later stages of spermiogenesis during flagellum elongation in spermatids. Varying degrees of *Prss50*-null sperm tail morphologies exist, ranging in severity from bent tails to the more severe 'conjoined' phenotype. The conjoined sperm phenotype represents a novel sperm morphology in the literature. Surprisingly, the conjoined sperm were able to move but in a static manner because the two heads appear to be pulling in opposite directions. TEM indicated that two sperm tails can be enclosed in the same plasma membrane (Fig. 4R). In *Prss50*-null sperm, a delay in cell division could allow two adjacent spermatids to begin to elongate and transform into elongated spermatids without separating their plasma membrane. We speculate that the conjoined sperm could be two sperm trapped in the same plasma membrane, indicating a failure in cell division, which could also explain sperm with multiple heads and midpieces but only one principal piece. Extra centrosomes can also give rise to more than one flagellum per cell (Barrera et al., 2010). Furthermore, failures in cytokinesis can result in the accumulation of more than two centrosomes per cell (centrosome amplification) (Doxsey, 2002), producing sperm with multiple centrosomes, heads and midpieces but with two principal pieces in the same membrane.

During spermatogenesis, the primary role of the centrosome is to ensure cytokinesis and subsequent cell cycle progression (Khodjakov and Rieder, 2001; Piel et al., 2001). In the cytoplasm of round spermatids, the pair of centrioles in the centrosome forms the neck or connecting piece (Lehti and Sironen, 2017). The proximal centriole migrates towards the spermatid nucleus and attaches to it in the implantation fossa; then, microtubules are recruited to the distal centriole surrounded by pericentriolar material to form the sperm tail axoneme (Wojcik et al., 2000; Sutovsky et al., 2004; Rawe et al., 2008; Pleuger et al., 2020). Most *Prss50*-null sperm had a fragile connection between the head and the tail, and presented with acephalic morphology. The fragile connection between the head and tail in *Prss50*-null sperm suggested a defect in the centrosome and/or centrioles, which we observed by TEM. The proper head-midpiece connection is important for fertility. This has been shown in the context of poor intracytoplasmic sperm injection outcomes, where improper connections resulting in acephalic or misaligned head-midpiece sperm as a result of dysfunctional centrioles cause breaks between the head and tail or at the midpiece with subsequent impaired fertility (Baccetti et al., 1989; Chemes et al., 1999; Saïas-Magnan et al., 1999; Rawe et al., 2002). If the centriole fails to establish proper contact with the nucleus, the head and tail will separate at spermiation. When the centriole attaches to the nucleus away from the longitudinal axis that extends from the center of the acrosome to the caudal pole of the spermatid nucleus, the heads and tails will not be aligned, and they will easily break away from each other. Both conditions generate acephalic sperm (Chemes and Alvarez Sedo, 2012). Both these defects are observed in *Prss50*-null mice, indicating that a defect in centriole attachment may cause the acephalic sperm phenotype as well as the sperm with one head and two full tails.

The signaling pathways by which PRSS50 acts in spermatogenesis are poorly understood. Thus, identifying molecular signaling networks responsible for the phenotype observed in *Prss50*-null mice remains challenging. We investigated the main mechanisms of action of PRSS50 in cancer cells. PRSS50 is a well-known regulator of IκB, an inhibitor of the NFκB signaling pathway (Zhang, 2014). In the absence of PRSS50, IκB levels increase, resulting in decreased levels of active NFκB (Zhang, 2014). Our model indicated a significant increase in IκB, suggesting that PRSS50 acts in the degradation of IκB to allow the activation of NFκB target genes. There are limited known targets of NFκB in the testis, but one of them is the centrosome protein LRWD1 (Teng et al., 2012), which is decreased in *Prss50*-null mice. The increase of IκB and decrease in LRWD1 are likely regulators of the phenotype observed in *Prss50*-null mice; however, we cannot rule out the possibility that a new regulatory pathway between PRSS50 and LRWD1 exists (Fig. 8G). In addition, NFκB downregulation in the testis of *Prss50*-null mice could affect other proteins involved in sperm morphogenesis, such as SEPT12. The IκB complex, in addition to acting as the signal integration hub for NFκB activation, could crosstalk with other pathways, triggering a wide variety of NFκB-independent signaling events, including proteasomal degradation and regulation of the mTOR, VEGF, EKR and CTNNB1 pathways (Hinz and Scheidereit, 2014). Given that IκB is involved in numerous physiological processes, the identification of PRSS50 as an upstream modulator of IκB activation in spermatogenesis has potential pharmacological relevance.

LRWD1 has multiple functions including: (1) promoting microtubule nucleation during G1; (2) acting as a scaffold to recruit and stabilize the ORC to chromatin to form the pre-replication complex during G1; and (3) binding to histones H3 and H4 to organize heterochromatin structure and silence satellite repeats (Bartke et al., 2010; Shen et al., 2010, 2012; Vermeulen et al., 2010; Chan and Zhang, 2012; Wang et al., 2018). LRWD1 is an important centriolar protein with significantly reduced levels in the neck of sperm from patients with asthenoteratozoospermia (Wang et al., 2018). Alterations of head-neck attachment and multiple tails observed in *Prss50*-null sperm could be attributable not only to abnormal centrosomal/centriolar organization, but also decreased levels of centrosome proteins, such as LRWD1. LRWD1 promotes proper microtubule nucleation, which occurs primarily at the centriole (Wang et al., 2018). We suspect that abnormal centriole-nuclear engagement is driven in part due to microtubule nucleation defects as a result of decreased LRWD1 levels. In addition, LRWD1 is recruited onto chromatin by interacting with repressive marks, such as H3K9me3 and methyl CpG sites. Reduction in LRWD1 protein levels correlates with decreased H3K9me3 and DNA methylation, which indicates a feedback loop between LRWD1 and repressive chromatin marks (Wang et al., 2017). In addition, LRWD1 functions as a scaffold protein that enables the formation of multiple histone complexes (Giri and Prasanth, 2015). Our data validate these *in vitro* results because the decrease in LRWD1 correlated with decreases in different histone methylation.

In spermiogenesis, the haploid spermatids undergo extensive morphological changes to achieve chromatin compaction. Histone variants are highly expressed in early round spermatids, and chromatin condensation results in transcriptional shutdown (Ernst et al., 2019). Proper methylation and demethylation of H3K9 is essential for the normal progression of spermatogenesis (Peters et al., 2001; Khalil et al., 2004). Alterations of H3K9 and H4K20 methylation are present in men with asthenoteratozoospermia (Schon et al., 2019). Progression of spermatogonia to meiosis was

Development (2021) 148, dev197558. doi:10.1242/dev.197558

severely limited in the absence of histone H3K4 demethylase KDM1A, as indicated in the Kdm1a-c-knockout (KO) mice (Lambrot et al., 2015). In these mice, spermatogonia are able to enter meiotic prophase, but are blocked in a zygotene-like state and quickly degenerate with loss of germ cells by P21. Loss of KDM1A was associated with altered histone H3 methylation and acetylation, and, more importantly, with upregulation of several meiotic factors, including Prss50 (2.7-fold), which suggests that the differentiation of germ cells is affected by histone alterations. Furthermore, changes in histone acetylation levels induced spermatid morphological abnormalities, including multinucleated syncytium formation (Dai et al., 2015) similar to that observed in *Prss50*-null mice. Based on our observations and those from other studies, our results suggest that the proper regulation of histone levels is important for spermatid differentiation. Histone modifications, including methylation at the early round spermatid stage, are involved in the repression of many genes, including the regulation of escape genes, such as *Akap4* (Ernst et al., 2019). In *Prss50*-null mice, we observed increased testicular AKAP4 protein levels. AKAP4 is expressed in the cytoplasm of round and elongated spermatids, being a marker of elongating cells (Hu et al., 2009; Green et al., 2018). AKAP4 is the major component of the fibrous sheath of the principal piece of the sperm flagellum, which first appears in round spermatids. The formation of the definitive fibrous sheath occurs near the end of spermiogenesis (Miki et al., 2002). Given that spermatogenesis occurs under strict regulation, overexpression of AKAP4 may contribute to the sperm anomalies observed in our mouse model.

The molecular mechanisms of most MMAF-related genes are still poorly understood, but several include defects along the tail, including the axoneme (DNAH1 and WDR66), the peri-axonemal structures (AKAP and FSIP2), the axonemo-periaxonemal space (CFAP43 and CFAP44) and the midpiece (CFAP69) (Touré et al., 2020; Wang et al., 2020). Our study highlights proteases, in particular PRSS50, as being important in the MMAF pathology. We developed several novel high-capacity algorithms, which enabled us to characterize the abnormal sperm phenotypes in a high-throughput unbiased fashion. In infertile men, detection of flagellar abnormities has improved with the standardized criteria of sperm analysis using the *WHO Laboratory Manual for the Examination and Processing of Human Semen* (5th edn). For some men to have an appropriate MMAF diagnostic workup, TEM examination is required, which is prohibitive both technically and in terms of cost in many clinical environments (Wang et al., 2020). The automated approach developed in this work has significant clinical applications, given the wide variability between labs regarding morphology testing (Keel et al., 2000) and the possibility of obtaining a diagnosis of MMAF without performing expensive and sophisticated tests, such as TEM.

This work emphasizes the complexity of the protein networks and molecular mechanisms that govern sperm flagellum assembly and organization. The loss of *Prss50* results in abnormal sperm tail development. The targets for PRSS50 remain mostly unknown, although current data support the activation of the NFκB pathways and centrosome proteins, such as LRWD1. Genetic variants in genes important in sperm morphology altered in our model, such *Lrwd1*, *Akap4* and *Sept12*, are associated with male infertility (Chemes and Rawe, 2003; Baccetti et al., 2005; Lin et al., 2012; Miyamoto et al., 2014; Wang et al., 2018). Although men with MMAF can fertilize eggs through intracytoplasmic sperm injection, aneuploidy and low implantation rates have been reported that are influenced by the type of ultrastructural flagellar defects carried by the patients (Coutton et al., 2015). Fertilization failure and abnormal embryonic development reported in patients with MMAF might be caused by defects in centrosomal or pericentrosomal proteins (Sathananthan, 1994; Chemes and Alvarez Sedo, 2012). Ultimately, the current study and that of others will establish the genes responsible for MMAF, enabling diagnosis by molecular panels, guided treatment options and perhaps genetic counseling tailored to specific mechanistic defects.

MATERIALS AND METHODS

Generation of mice

All experiments were approved by our Institutional Animal Care and Use Committee (IACUC) at Baylor College of Medicine (BCM). *Prss50*-null mice were generated by the Genetically Engineered Mouse Core at BCM using CRISPR/Cas9 (Fig. S1). We used CRISPR/Cas9 genome editing to cause a frame shift in exon 2 that produced a premature stop codon used as 5′ guide sequence (AGAAAAGGTTGGGTAGCTAC AGG) and a 3′ guide sequence (TTGCTACTTGATGGGTCACC TGG). Homozygote mice in a C57BL/6J background were viable and fertile. Mice were genotyped using the following PCR primers (F: gcccaagctgtaggaacaag; R: aacccaaggaaggaacctgt.) The WT allele produces a 581 bp band, and the *Prss50*-null allele produces a 200 bp band. We confirmed the *Prss50*-null alleles by western blot and IHC.

Fertility analysis

We assessed the fertility of *Prss50*-null mice by longitudinal breeding (6 months). Mice were housed under a 12 h light/12 h dark cycle and received diet and water *ad libitum*. Each WT (C57BL/6J) and *Prss50*-null male (n=10 in each group) was housed with one WT female for 8 months, beginning at 6 weeks of age. During this period, we recorded the number of litters and the number of pups produced from each breeding pair. After 6 months of mating, we euthanized the male mice, and body, testis and epididymal weights were recorded and analyzed.

Testis histology and sperm staining

Specimens from human subjects were obtained following informed consent by the participants. This study was approved by, and conducted under the oversight of, the Institutional Review Board of BCM. All mouse experiments were executed in accordance with institutional guidelines and were approved by the IACUC at BCM. We harvested the testis and caput epididymis from male mice at the time of sacrifice. Tissue was placed in Bouin's solution (Ricca Chemical, Cat 1120-32) for fixation for 5 h at room temperature and then transferred to 70% ethanol before dehydration and paraffin embedding. Tissue was sectioned at 5 µm. Periodic acid–Schiff (PAS) staining was performed by the Pathology Core and Lab at BCM. For IHC, sections were deparaffinized, and antigens were retrieved for 10 min in sodium citrate buffer (pH 6). Slides were incubated in 3% hydrogen peroxide in PBS for 10 min to neutralize endogenous peroxidase. Sections were blocked using 2.5% horse serum (Vector Laboratories: S-2000). Primary antibodies were incubated overnight at 4°C. Primary antibodies and dilutions were as follows: anti-TSP50 (1:100; R&D AF2455), anti-PLZF (1:200; Abcam 189849), anti-AR (1:150; Santa Cruz Biotechnology 816), anti-CDK1 (1:500; Abcam 131450), anti-3β-HSD (1:150; Santa Cruz Biotechnology SC30820), anti-Ki67 (1:150; Abcam 16667) and anti-TEX14 (1:500; a gift from Dr Martin Matzuk, Center for Drug Discovery, BCM). Antibody detection was obtained using the ImmPRESS Horseradish Peroxidase (HRP) Polymer Reagents (Vector Laboratories MP-7401 for rabbit antibodies and MP-7405 for goat antibodies). Staining was performed using DAB Kit (Vector Laboratories SK-4100), and sections were counterstained using Hematoxylin and Eosin (H&E). For IF, antigen retrieval was performed as above, and sections were incubated in primary antibodies overnight at 4°C. Primary antibodies and dilutions were as follows: anti-tri-methyl-histone H3 (Lys9) (1:200; Abcam 176916), anti-SEPT12 (1:100; Invitrogen PA5-31504), anti-AKAP4 (1:200; 4BioDx, 4BDX-1602) and anti-α-tubulin (1:200; Abcam 24610). Slides were mounted using Permount for IHC and with ProLong Diamond Antifade Mountant with DAPI (ThermoFisher P36962) for immunofluorescence. The sections were examined at different magnifications using an Olympus BX51 microscope and its associated software cellSens. For super-resolution images, the GE HealthCare DeltaVision OMX, a 3D structured illumination

Development (2021) 148, dev197558. doi:10.1242/dev.197558

microscope (3D-SIM), was used to obtain highly stable, multi-channel imaging. For confocal imaging, the super resolution IXplore Spin XR from Olympus was used.

Western blot

Whole-cell lysates from testes were collected using Tissue Protein Extraction Reagent (Thermo Fisher Scientific 78510) that was supplemented with complete mini protease inhibitor (Roche 11836153001). Tissue lysis was performed at 4°C for 30 min on a rocking shaker, and the supernatant fraction was collected following centrifugation at 10,000 ***g*** for 5 min at 4°C. Protein quantification was performed using the Pierce BCA Protein Assay Kit (Thermo Fisher Scientific 23225). Next, 30 µg of protein per well was run and transferred to a PVDF membrane. Blots were blocked and primary antibodies were incubated overnight at 4°C as per the manufacturer's instructions. Primary antibodies and dilutions were as follows: anti-TSP50 (1:1000; R&D AF2455), anti-LRWD1 (1:1000; Protein Tech 19546-1-AP), anti-TEX14 (1:1000), anti-IKKB (1:1000; CST 8943), anti-gamma H2A.X (phospho-S139) (1:1000; Abcam ab81299), anti-Histone H3.3 (1:1000; Abcam ab176840), mono-methyl-histone H3 (Lys9) (1:1000; CST 14186), tri-methyl-histone H3 (Lys9) (1:1000; CST 13969), anti-AKAP4 (1:1000; Invitrogen PA5-38015) and anti-SOX9 (1:1000; Abcam ab185230). Anti-β-actin at 1:2000 (CST 12620) and anti-GAPDH-HRP conjugate at 1:1000 (CST 8884) were used as loading controls. Goat anti-rabbit IgG (H+L)-HRP conjugate (1:1000; BIORAD 170-6515) secondary antibodies were used as per the manufacturer's instructions. Images were acquired with the ChemidocTM Touch Imaging System (BIORAD 1708370,) and its associated software, Image Lab Touch version 1.2. Western blot band intensity was analyzed using the freely available software NIH Image J (http://imagej.nih.gov/ij/).

Sperm analysis

Each caudal epididymis was placed in 1 ml of pre-warmed Embryo-max HTF media (Millipore-Sigma MR-070-D). The epididymis was cut five times, and the sperm were allowed to swim into the media at 37°C for 15 min. Following incubation, the sperm were diluted 1:50 in HTF media, added to a pre-warmed slide and analyzed with computer-assisted sperm analysis (CASA) using Hamilton-Thorne Bioscience's Ceros II software program. Several ($n \geq 6$) fields of view were illuminated and captured until at least 600 cells were counted. To label the midpiece of the sperm, sperm were incubated with 200 nM MitoTracker Deep Red (Thermo Fisher Scientific M22426) for 30 min in 450 µl of sterile PBS at 37°C. Then, 25 µl of sperm in PBS was smeared across slides and allowed to air dry. Sperm smears were fixed with 4% PFA overnight at 4°C and washed three times with PBS. For IF, MitoTracker Deep Red-labeled sperm were blocked with 10% donkey serum and incubated with primary antibody in 1% donkey serum overnight at 4°C. Primary antibodies and dilutions were as follows: anti-α-tubulin (1:200) and anti-SEPT12 (1:200). Slides were mounted using anti-fade mounting medium with DAPI (Thermo Fisher Scientific P36962). Images were taken using a super-resolution microscope. Annulus number was scored for the number of SEPT12 signals that were identified at the neck or midpiece, or both. SEPT12 scoring was performed blinded to genotype.

High content analysis of sperm morphology

After sperm were labeled with MitoTracker Deep Red, they were washed once using 500 µl sterile PBS and 50 µl of sperm were transferred into four replicate wells of a 96-well glass-bottom plate. Samples were allowed to air dry and then fixed using a 4% electromicroscopy (EM)-grade paraformaldehyde PBS solution for 30 min at room temperature. Samples were permeabilized using a 0.5% Triton-X PBS solution and then blocked using a blotto solution (5% powdered milk in TBS-T buffer). Samples were incubated with primary anti-α-tubulin antibody (1:2000) overnight at 4°C. Samples were then washed using TBS-T buffer and then incubated for 60 min at room temperature with secondary anti-rabbit Alexa 488 antibody solution. DNA was labeled using a 1 µg/ml DAPI solution prepared in PBS. Samples were imaged using an IC200 image cytometer (Vala Sciences) equipped with a 40× objective. In total, 40 fields per well were collected in 3D and then projected using a synthetic focus algorithm. A minimum of 10,000 sperm per sample were imaged. Images were analyzed using an algorithm developed within the myImageAnalysis web application (Szafran and Mancini, 2014). Using an algorithm developed initially for neuronal segmentation, sperm head (DAPI), midpiece (MitoTracker Deep Red FM Invitrogen M22426) and tail (α-tubulin) were segmented, and quantitative features extracted. A rule-based classification method based on morphological features was applied to characterize differences observed in the sperm samples.

High content analysis of sperm mitochondria

Mouse sperm samples were loaded with JC-1 dye by incubating in HTF media containing 2 µM JC-1 and 20 µg/ml Hoechst dye. A replicate set containing JC-1, Hoechst and 100 µM CCCP was also prepared. Sperm were incubated for 60 min prior to washing, resuspended in a 50/50 mix of HTF media/sterile glycerol and transferred to a 96-well glass-bottom plate. The plate was briefly spun to settle sperm to the bottom of the wells. Samples were imaged using a Vala Sciences IC200 image cytometer equipped with a Nikon 40X/0.95 Pan-Apo objective. Signals were captured using excitation/emission wavelengths of 350/455 nM (Hoechst), 490/525 nM (JC-1 Green) and 490/605 nM (JC-1 Red). Fifteen fields from each well were analyzed using the myImageAnalysis application. The sperm head regions were defined by the Hoechst label, and the mitochondrial regions were defined by the JC-1 label. Features describing the morphology and the Hoechst, JC-1 Green and JC-1 Red signal intensity of each region were collected for each analyzed sperm. Manual inspection of the images demonstrated two predominant mitochondrial morphology patterns. To determine the frequency of each pattern in the sperm samples, a cross-validated random forest artificial intelligence model was trained with 200 manually selected examples of each pattern. After two rounds of training, the model achieved a receiver operating characteristic area under the curve (ROC AUC) greater than 0.9, indicating a high degree of accuracy.

High content analysis of sperm chromatin structure

Sperm were collected from the caudal epididymis in HTF media and stored in a 37°C incubator for 30 min before processing. Sperm were denatured using a low pH TNA solution (0.1% Triton-X100, 0.15 M NaCl, pH 1.4 using HCl) and then labeled with 10 µg/ml Acridine Orange (AO) in PBS solution. Sperm were then plated into a 96-well plate, spun and then imaged using the IC200 instrument equipped with a 40× objective. In total, 20 fields per well were imaged, capturing the AO-Green and AO-Red signals. Images were analyzed using the myImageAnalysis application to remove background signal and identify each labeled sperm head. Objects were filtered to remove non-biological artifacts and objects touching the edge of the imaged region; intensity and shape features were collected on a per sperm basis. HCA-SCSA generates metrics analogous to standard flow cytometry-based SCSA, including the percent of sperm with high DNA stainability (% HDS, an indicator of low protamine exchange and/or immature sperm) and percent of sperm with high DNA fragmentation index (% DFI, a ratio of red-to-green signal intensity).

Electron microscopy

Testis and epididymis were dissected from animals, placed immediately in cold drops of modified Karnovsky's fixative (Karnovsky, 1965), and processed and imaged as previously published (Jorgez et al., 2021).

Statistical analysis

Data are presented as mean±s.e.m. or s.d., and were analyzed using one-way ANOVA with Bonferroni correction using GraphPad Prism. $P<0.01$ was considered statistically significant.

Acknowledgements

Support provided by the Integrated Microscopy Core was by funding by the John S. Dunn Gulf Coast Consortium for Chemical Genomics, the Dan L. Duncan Cancer Center (P30CA125123) and the National Institutes of Health (HD007495 and DK56338). The Pathology Core is supported by the National Institutes of Health (P30 NCI-CA125123).

Competing interests

The authors declare no competing or financial interests.

Author contributions

Conceptualization: J.M.S., J.C.B., A.T.S., M.S., J.M., C.H.C., J.Z., N.W., A.S., C.J.J.; Methodology: J.M.S., J.C.B., A.T.S., M.S., J.M., A.R., C.H.C., J.Z., N.W., C.J.J.; Software: A.T.S., C.J.J.; Validation: J.M.S., J.C.B., A.T.S., M.S., J.M., A.R., C.H.C., J.Z., N.W., C.J.J.; Formal analysis: J.M.S., J.C.B., A.T.S., M.S., J.M., A.R., C.H.C., J.Z., N.W., A.S., C.J.J.; Investigation: J.M.S., J.C.B., A.T.S., M.S., J.M., A.R., C.H.C., J.Z., N.W., A.S., C.J.J.; Resources: A.T.S., N.W., A.S., C.J.J.; Data curation: J.M.S., J.C.B., A.T.S., J.M., A.R., J.Z., N.W., A.S., C.J.J.; Writing - original draft: J.M.S., J.C.B., A.T.S., M.S., J.M., A.R., C.H.C., J.Z., N.W., A.S., C.J.J.; Writing - review & editing: J.M.S., J.C.B., A.T.S., M.S., J.M., A.R., C.H.C., J.Z., N.W., A.S., C.J.J.; Visualization: J.M.S., J.C.B., J.Z., C.J.J.; Supervision: J.C.B., A.S., C.J.J.; Project administration: A.S., C.J.J.; Funding acquisition: A.S., C.J.J.

Funding

The authors' research is supported by the National Institute of Health (NIH). C.J.J. and A.S. are supported, in part, by the Eunice Kennedy Shriver National Institute of Child Health and Human Development (1R01HD100985). J.M.S. was a fellow of National Institute of General Medical Sciences (T32GM088129). A.Z., A.S. and C.J.J. were K12 scholars of the Multidisciplinary K12 Urologic Research (KURe) Career Development Program (K12DK0083014). Deposited in PMC for release after 12 months.

References

Adams, S. R., Maezawa, S., Alavattam, K. G., Abe, H., Sakashita, A., Shroder, M., Broering, T. J., Sroga Rios, J., Thomas, M. A., Lin, X. et al. (2018). RNF8 and SCML2 cooperate to regulate ubiquitination and H3K27 acetylation for escape gene activation on the sex chromosomes. *PLoS Genet.* **14**, e1007233. doi:10.1371/journal.pgen.1007233

Baccetti, B., Burrini, A. G., Collodel, G., Magnano, A. R., Piomboni, P., Renieri, T. and Sensini, C. (1989). Morphogenesis of the decapitated and decaudated sperm defect in two brothers. *Gamete Res.* **23**, 181-188. doi:10.1002/mrd.1120230205

Baccetti, B., Collodel, G., Estenoz, M., Manca, D., Moretti, E. and Piomboni, P. (2005). Gene deletions in an infertile man with sperm fibrous sheath dysplasia. *Hum. Reprod.* **20**, 2790-2794. doi:10.1093/humrep/dei126

Barrera, J. A., Kao, L.-R., Hammer, R. E., Seemann, J., Fuchs, J. L. and Megraw, T. L. (2010). CDK5RAP2 regulates centriole engagement and cohesion in mice. *Dev. Cell* **18**, 913-926. doi:10.1016/j.devcel.2010.05.017

Bartke, T., Vermeulen, M., Xhemalce, B., Robson, S. C., Mann, M. and Kouzarides, T. (2010). Nucleosome-interacting proteins regulated by DNA and histone methylation. *Cell* **143**, 470-484. doi:10.1016/j.cell.2010.10.012

Ben Khelifa, M., Coutton, C., Zouari, R., Karaouzène, T., Rendu, J., Bidart, M., Yassine, S., Pierre, V., Delaroche, J., Hennebicq, S. et al. (2014). Mutations in DNAH1, which encodes an inner arm heavy chain dynein, lead to male infertility from multiple morphological abnormalities of the sperm flagella. *Am. J. Hum. Genet.* **94**, 95-104. doi:10.1016/j.ajhg.2013.11.017

Cao, Q.-H., Liu, F., Li, C.-Z., Liu, N., Shu, M., Lin, Y., Ding, L. and Xue, L. (2018). Testes-specific protease 50 (TSP50) promotes invasion and metastasis by inducing EMT in gastric cancer. *BMC Cancer* **18**, 94. doi:10.1186/s12885-018-4000-y

Chan, K. M. and Zhang, Z. (2012). Leucine-rich repeat and WD repeat-containing protein 1 is recruited to pericentric heterochromatin by trimethylated lysine 9 of histone H3 and maintains heterochromatin silencing. *J. Biol. Chem.* **287**, 15024-15033. doi:10.1074/jbc.M111.337980

Chemes, H. E. and Alvarez Sedo, C. (2012). Tales of the tail and sperm head aches: changing concepts on the prognostic significance of sperm pathologies affecting the head, neck and tail. *Asian J. Androl.* **14**, 14-23. doi:10.1038/aja.2011.168

Chemes, E. H. and Rawe, Y. V. (2003). Sperm pathology: a step beyond descriptive morphology. Origin, characterization and fertility potential of abnormal sperm phenotypes in infertile men. *Hum. Reprod. Update* **9**, 405-428. doi:10.1093/humupd/dmg034

Chemes, H. E., Puigdomenech, E. T., Carizza, C., Olmedo, S. B., Zanchetti, F. and Hermes, R. (1999). Acephalic spermatozoa and abnormal development of the head-neck attachment: a human syndrome of genetic origin. *Hum. Reprod.* **14**, 1811-1818. doi:10.1093/humrep/14.7.1811

Clement, T. M., Inselman, A. L., Goulding, E. H., Willis, W. D. and Eddy, E. M. (2015). Disrupting cyclin dependent kinase 1 in spermatocytes causes late meiotic arrest and infertility in mice. *Biol. Reprod.* **93**, 137. doi:10.1095/biolreprod.115.134940

Conway, G. D., Buzza, M. S., Martin, E. W., Duru, N., Johnson, T. A., Peroutka, R. J., Pawar, N. R. and Antalis, T. M. (2019). PRSS21/testisin inhibits ovarian tumor metastasis and antagonizes proangiogenic angiopoietins ANG2 and ANGPTL4. *J. Mol. Med. (Berl.)* **97**, 691-709. doi:10.1007/s00109-019-01763-3

Coutton, C., Escoffier, J., Martinez, G., Arnoult, C. and Ray, P. F. (2015). Teratozoospermia: spotlight on the main genetic actors in the human. *Hum. Reprod. Update* **21**, 455-485. doi:10.1093/humupd/dmv020

Dai, L., Endo, D., Akiyama, N., Yamamoto-Fukuda, T. and Koji, T. (2015). Aberrant levels of histone H3 acetylation induce spermatid anomaly in mouse testis. *Histochem. Cell Biol.* **143**, 209-224. doi:10.1007/s00418-014-1283-1

Datta, J., Palmer, M. J., Tanton, C., Gibson, L. J., Jones, K. G., Macdowall, W., Glasier, A., Sonnenberg, P., Field, N., Mercer, C. H. et al. (2016). Prevalence of infertility and help seeking among 15,000 women and men. *Hum. Reprod.* **31**, 2108-2118. doi:10.1093/humrep/dew123

Doxsey, S. (2002). Duplicating dangerously: linking centrosome duplication and aneuploidy. *Mol. Cell* **10**, 439-440. doi:10.1016/S1097-2765(02)00654-8

Ernst, C., Eling, N., Martinez-Jimenez, C. P., Marioni, J. C. and Odom, D. T. (2019). Staged developmental mapping and X chromosome transcriptional dynamics during mouse spermatogenesis. *Nat. Commun.* **10**, 1251. doi:10.1038/s41467-019-09182-1

Forti, G. and Krausz, C. (1998). Clinical review 100, Evaluation and treatment of the infertile couple. *J. Clin. Endocrinol. Metab.* **83**, 4177-4188. doi:10.1210/jc.83.12.4177

Giri, S. and Prasanth, S. G. (2015). Association of ORCA/LRWD1 with repressive histone methyl transferases mediates heterochromatin organization. *Nucleus* **6**, 435-441. doi:10.1080/19491034.2015.1102814

Gopinathan, L., Szmyd, R., Low, D., Diril, M. K., Chang, H. Y., Coppola, V., Liu, K., Tessarollo, L., Guccione, E., van Pelt, A. MM. et al. (2017). Emi2 Is Essential for Mouse Spermatogenesis. *Cell Rep.* **20**, 697-708. doi:10.1016/j.celrep.2017.06.033

Green, C. D., Ma, Q., Manske, G. L., Shami, A. N., Zheng, X., Marini, S., Moritz, L., Sultan, C., Gurczynski, S. J., Moore, B. B. et al. (2018). A comprehensive roadmap of murine spermatogenesis defined by single-cell RNA-seq. *Dev. Cell* **46**, 651-667.e610. doi:10.1016/j.devcel.2018.07.025

Hinz, M. and Scheidereit, C. (2014). The IκB kinase complex in NF-κB regulation and beyond. *EMBO Rep.* **15**, 46-61. doi:10.1002/embr.201337983

Hu, Y., Yu, H., Pask, A. J., O'Brien, D. A., Shaw, G. and Renfree, M. B. (2009). A-kinase anchoring protein 4 has a conserved role in mammalian spermatogenesis. *Reproduction* **137**, 645-653. doi:10.1530/REP-08-0337

Jordan, P. W., Karppinen, J. and Handel, M. A. (2012). Polo-like kinase is required for synaptonemal complex disassembly and phosphorylation in mouse spermatocytes. *J. Cell Sci.* **125**, 5061-5072. doi:10.1242/jcs.105015

Jorgez, C. J., Seth, A., Wilken, N., Bournat, J. C., Chen, C. H. and Lamb, D. J. (2021). E2F1 regulates testicular descent and controls spermatogenesis by influencing WNT4 signaling. *Development* **148**, dev191189. doi:10.1242/dev.191189

Karnovsky, M. J. (1965). A formaldehyde-glutaraldehyde fixative of high osmolality for use in electron-microscopy. *J. Cell Biol.* **27**, 137-138.

Keel, B. A., Quinn, P., Schmidt, C. F., Jr, Serafy, N. T., Jr, Serafy, N. T., Sr and Schalue, T. K. (2000). Results of the American Association of Bioanalysts national proficiency testing programme in andrology. *Hum. Reprod.* **15**, 680-686. doi:10.1093/humrep/15.3.680

Khalil, A. M., Boyar, F. Z. and Driscoll, D. J. (2004). Dynamic histone modifications mark sex chromosome inactivation and reactivation during mammalian spermatogenesis. *Proc. Natl. Acad. Sci. USA* **101**, 16583-16587. doi:10.1073/pnas.0406325101

Khodjakov, A. and Rieder, C. L. (2001). Centrosomes enhance the fidelity of cytokinesis in vertebrates and are required for cell cycle progression. *J. Cell Biol.* **153**, 237-242. doi:10.1083/jcb.153.1.237

Kimmins, S., Crosio, C., Kotaja, N., Hirayama, J., Monaco, L., Höög, C., van Duin, M., Gossen, J. A. and Sassone-Corsi, P. (2007). Differential functions of the Aurora-B and Aurora-C kinases in mammalian spermatogenesis. *Mol. Endocrinol.* **21**, 726-739. doi:10.1210/me.2006-0332

Kuo, P.-L., Chiang, H.-S., Wang, Y.-Y., Kuo, Y.-C., Chen, M.-F., Yu, I.-S., Teng, Y.-N., Lin, S.-W. and Lin, Y.-H. (2013). SEPT12-microtubule complexes are required for sperm head and tail formation. *Int. J. Mol. Sci.* **14**, 22102-22116. doi:10.3390/ijms141122102

Kuo, Y.-C., Shen, Y.-R., Chen, H.-I., Lin, Y.-H., Wang, Y.-Y., Chen, Y.-R., Wang, C.-Y. and Kuo, P.-L. (2015). SEPT12 orchestrates the formation of mammalian sperm annulus by organizing core octameric complexes with other SEPT proteins. *J. Cell Sci.* **128**, 923-934. doi:10.1242/jcs.158998

Lambrot, R., Lafleur, C. and Kimmins, S. (2015). The histone demethylase KDM1A is essential for the maintenance and differentiation of spermatogonial stem cells and progenitors. *FASEB J.* **29**, 4402-4416. doi:10.1096/fj.14-267328

Lehti, M. S. and Sironen, A. (2017). Formation and function of sperm tail structures in association with sperm motility defects. *Biol. Reprod.* **97**, 522-536. doi:10.1093/biolre/iox096

Lin, Y.-H., Lin, Y.-M., Teng, Y.-N., Hsieh, T.-Y. T., Lin, Y.-S. and Kuo, P.-L. (2006). Identification of ten novel genes involved in human spermatogenesis by microarray analysis of testicular tissue. *Fertil. Steril.* **86**, 1650-1658. doi:10.1016/j.fertnstert.2006.04.039

Lin, Y.-H., Wang, Y.-Y., Chen, H.-I., Kuo, Y.-C., Chiou, Y.-W., Lin, H.-H., Wu, C.-M., Hsu, C.-C., Chiang, H.-S. and Kuo, P.-L. (2012). SEPTIN12 genetic variants confer susceptibility to teratozoospermia. *PLoS ONE* **7**, e34011. doi:10.1371/journal.pone.0034011

Liu, F., Cao, Q., Liu, N., Li, C., You, C., Liu, C., Xue, L. and Luo, R. (2014). Overexpression of testes-Specific Protease 50 (TSP50) predicts poor prognosis

in patients with gastric cancer. *Gastroenterol. Res. Pract.* **2014**, 498246. doi:10.1155/2014/498246

Liu, J., Shen, C., Fan, W., Chen, Y., Zhang, A., Feng, Y., Li, Z., Kuang, Y. and Wang, Z. (2016). Low levels of PRSS37 protein in sperm are associated with many cases of unexplained male infertility. *Acta Biochim. Biophys. Sin (Shanghai)* **48**, 1058-1065. doi:10.1093/abbs/gmw096

McCarrey, J. R. (2013). Toward a more precise and informative nomenclature describing fetal and neonatal male germ cells in rodents. *Biol. Reprod.* **89**, 47. doi:10.1095/biolreprod.113.110502

Miki, K., Willis, W. D., Brown, P. R., Goulding, E. H., Fulcher, K. D. and Eddy, E. M. (2002). Targeted disruption of the Akap4 gene causes defects in sperm flagellum and motility. *Dev. Biol.* **248**, 331-342. doi:10.1006/dbio.2002.0728

Miyamoto, T., Koh, E., Tsujimura, A., Miyagawa, Y., Saijo, Y., Namiki, M. and Sengoku, K. (2014). Single-nucleotide polymorphisms in the LRWD1 gene may be a genetic risk factor for Japanese patients with Sertoli cell-only syndrome. *Andrologia* **46**, 273-276. doi:10.1111/and.12077

Morton, D., Weisbrode, S. E., Wyder, W. E., Maurer, J. K. and Capen, C. C. (1986). Spermatid giant cells, tubular hypospermatogenesis, spermatogonial swelling, cytoplasmic vacuoles, and tubular dilatation in the testes of normal rabbits. *Vet. Pathol.* **23**, 176-183. doi:10.1177/030098588602300211

Nebel, B. R., Amarose, A. P. and Hacket, E. M. (1961). Calendar of gametogenic development in the prepuberal male mouse. *Science* **134**, 832-833. doi:10.1126/science.134.3482.832

Netzel-Arnett, S., Bugge, T. H., Hess, R. A., Carnes, K., Stringer, B. W., Scarman, A. L., Hooper, J. D., Tonks, I. D., Kay, G. F. and Antalis, T. M. (2009). The glycosylphosphatidylinositol-anchored serine protease PRSS21 (testisin) imparts murine epididymal sperm cell maturation and fertilizing ability. *Biol. Reprod.* **81**, 921-932. doi:10.1095/biolreprod.109.076273

O'Donnell, L. (2014). Mechanisms of spermiogenesis and spermiation and how they are disturbed. *Spermatogenesis* **4**, e979623. doi:10.4161/21565562.2014.979623

O'Donnell, L., Rhodes, D., Smith, S. J., Merriner, D. J., Clark, B. J., Borg, C., Whittle, B., O'Connor, A. E., Smith, L. B., McNally, F. J. et al. (2012). An essential role for katanin p80 and microtubule severing in male gamete production. *PLoS Genet.* **8**, e1002698. doi:10.1371/journal.pgen.1002698

Peters, A. H. F. M., O'Carroll, D., Scherthan, H., Mechtler, K., Sauer, S., Schöfer, C., Weipoltshammer, K., Pagani, M., Lachner, M., Kohlmaier, A. et al. (2001). Loss of the Suv39h histone methyltransferases impairs mammalian heterochromatin and genome stability. *Cell* **107**, 323-337. doi:10.1016/S0092-8674(01)00542-6

Piel, M., Nordberg, J., Euteneuer, U. and Bornens, M. (2001). Centrosome-dependent exit of cytokinesis in animal cells. *Science* **291**, 1550-1553. doi:10.1126/science.1057330

Pleuger, C., Lehti, M. S., Dunleavy, J. E. M., Fietz, D. and O'Bryan, M. K. (2020). Haploid male germ cells-the Grand Central Station of protein transport. *Hum. Reprod. Update* **26**, 474-500. doi:10.1093/humupd/dmaa004

Rawe, V. Y., Terada, Y., Nakamura, S., Chillik, C. F., Olmedo, S. B. and Chemes, H. E. (2002). A pathology of the sperm centriole responsible for defective sperm aster formation, syngamy and cleavage. *Hum. Reprod.* **17**, 2344-2349. doi:10.1093/humrep/17.9.2344

Rawe, V. Y., Diaz, E. S., Abdelmassih, R., Wojcik, C., Morales, P., Sutovsky, P. and Chemes, H. E. (2008). The role of sperm proteasomes during sperm aster formation and early zygote development: implications for fertilization failure in humans. *Hum. Reprod.* **23**, 573-580. doi:10.1093/humrep/dem385

Saïas-Magnan, J., Metzler-Guillemain, C., Mercier, G., Carles-Marcorelles, F., Grillo, J. M. and Guichaoua, M. R. (1999). Failure of pregnancy after intracytoplasmic sperm injection with decapitated spermatozoa: case report. *Hum. Reprod.* **14**, 1989-1992. doi:10.1093/humrep/14.8.1989

Sathananthan, A. H. (1994). Functional competence of abnormal spermatozoa. *Bailliere's clinical obstetrics and gynaecology* **8**, 141-156. doi:10.1016/S0950-3552(05)80029-X

Schon, S. B., Luense, L. J., Wang, X., Bartolomei, M. S., Coutifaris, C., Garcia, B. A. and Berger, S. L. (2019). Histone modification signatures in human sperm distinguish clinical abnormalities. *J. Assist. Reprod. Genet.* **36**, 267-275. doi:10.1007/s10815-018-1354-7

Shang, X., Shen, C., Liu, J., Tang, L., Zhang, H., Wang, Y., Wu, W., Chi, J., Zhuang, H., Fei, J. et al. (2018). Serine protease PRSS55 is crucial for male mouse fertility via affecting sperm migration and sperm-egg binding. *Cell. Mol. Life Sci.* **75**, 4371-4384. doi:10.1007/s00018-018-2878-9

Sharlip, I. D., Jarow, J. P., Belker, A. M., Lipshultz, L. I., Sigman, M., Thomas, A. J., Schlegel, P. N., Howards, S. S., Nehra, A., Damewood, M. D. et al. (2002). Best practice policies for male infertility. *Fertil. Steril.* **77**, 873-882. doi:10.1016/S0015-0282(02)03105-9

Shen, Z., Sathyan, K. M., Geng, Y., Zheng, R., Chakraborty, A., Freeman, B., Wang, F., Prasanth, K. V. and Prasanth, S. G. (2010). A WD-repeat protein stabilizes ORC binding to chromatin. *Mol. Cell* **40**, 99-111. doi:10.1016/j.molcel.2010.09.021

Shen, Z., Chakraborty, A., Jain, A., Giri, S., Ha, T., Prasanth, K. V. and Prasanth, S. G. (2012). Dynamic association of ORCA with prereplicative complex components regulates DNA replication initiation. *Mol. Cell. Biol.* **32**, 3107-3120. doi:10.1128/MCB.00362-12

Shen, C., Kuang, Y., Liu, J., Feng, J., Chen, X., Wu, W., Chi, J., Tang, L., Wang, Y., Fei, J. et al. (2013). Prss37 is required for male fertility in the mouse. *Biol. Reprod.* **88**, 123. doi:10.1095/biolreprod.112.107086

Shen, Y.-R., Wang, H.-Y., Kuo, Y.-C., Shih, S.-C., Hsu, C.-H., Chen, Y.-R., Wu, S.-R., Wang, C.-Y. and Kuo, P.-L. (2017). SEPT12 phosphorylation results in loss of the septin ring/sperm annulus, defective sperm motility and poor male fertility. *PLoS Genet.* **13**, e1006631. doi:10.1371/journal.pgen.1006631

Song, Z.-B., Bao, Y.-L., Zhang, Y., Mi, X.-G., Wu, P., Wu, Y., Yu, C.-L., Sun, Y., Zheng, L.-H., Huang, Y.-X. et al. (2011). Testes-specific protease 50 (TSP50) promotes cell proliferation through the activation of the nuclear factor κB (NF-κB) signalling pathway. *Biochem. J.* **436**, 457-467. doi:10.1042/BJ20101780

Sutovsky, P., Manandhar, G., McCauley, T. C., Caamaño, J. N., Sutovsky, M., Thompson, W. E. and Day, B. N. (2004). Proteasomal interference prevents zona pellucida penetration and fertilization in mammals. *Biol. Reprod.* **71**, 1625-1637. doi:10.1095/biolreprod.104.032532

Szafran, A. T. and Mancini, M. A. (2014). The myImageAnalysis project: a web-based application for high-content screening. *Assay Drug Dev. Technol.* **12**, 87-99. doi:10.1089/adt.2013.532

Tan, M., Luo, H., Lee, S., Jin, F., Yang, J. S., Montellier, E., Buchou, T., Cheng, Z., Rousseaux, S., Rajagopal, N. et al. (2011). Identification of 67 histone marks and histone lysine crotonylation as a new type of histone modification. *Cell* **146**, 1016-1028. doi:10.1016/j.cell.2011.08.008

Teng, Y.-N., Liao, M.-H., Lin, Y.-B., Kuo, P.-L. and Kuo, T.-Y. (2010). Expression of lrwd1 in mouse testis and its centrosomal localization. *Int. J. Androl.* **33**, 832-840. doi:10.1111/j.1365-2605.2009.01038.x

Teng, Y.-N., Chuang, P.-J. and Liu, Y.-W. (2012). Nuclear factor-κB (NF-κB) regulates the expression of human testis-enriched Leucine-rich repeats and WD repeat domain containing 1 (LRWD1) gene. *Int. J. Mol. Sci.* **14**, 625-639. doi:10.3390/ijms14010625

Touré, A., Martinez, G., Kherraf, Z.-E., Cazin, C., Beurois, J., Arnoult, C., Ray, P. F. and Coutton, C. (2020). The genetic architecture of morphological abnormalities of the sperm tail. *Hum. Genet.* **40**, 21-42. doi:10.1007/s00439-020-02113-x

Vermeulen, M., Eberl, H. C., Matarese, F., Marks, H., Denissov, S., Butter, F., Lee, K. K., Olsen, J. V., Hyman, A. A., Stunnenberg, H. G. et al. (2010). Quantitative interaction proteomics and genome-wide profiling of epigenetic histone marks and their readers. *Cell* **142**, 967-980. doi:10.1016/j.cell.2010.08.020

Wang, Y., Khan, A., Marks, A. B., Smith, O. K., Giri, S., Lin, Y.-C., Creager, R., MacAlpine, D. M., Prasanth, K. V., Aladjem, M. I. et al. (2017). Temporal association of ORCA/LRWD1 to late-firing origins during G1 dictates heterochromatin replication and organization. *Nucleic Acids Res.* **45**, 2490-2502. doi:10.1093/nar/gkw1211

Wang, C. Y., Hong, Y. H., Syu, J. S., Tsai, Y. C., Liu, X. Y., Chen, T. Y., Su, Y. M., Kuo, P. L., Lin, Y. M. and Teng, Y. N. (2018). LRWD1 regulates microtubule nucleation and proper cell cycle progression in the human testicular embryonic carcinoma cells. *J. Cell. Biochem.* **119**, 314-326. doi:10.1002/jcb.26180

Wang, W.-L., Tu, C.-F. and Tan, Y.-Q. (2020). Insight on multiple morphological abnormalities of sperm flagella in male infertility: what is new? *Asian J. Androl.* **22**, 236-245. doi:10.4103/aja.aja_53_19

Wojcik, C., Benchaib, M., Lornage, J., Czyba, J. C. and Guerin, J. F. (2000). Proteasomes in human spermatozoa. *Int. J. Androl.* **23**, 169-177.

Wu, Z. G., Chen, W. K., Fei, Q. J., Liu, Y. L., Liu, X. D., Huang, H. and Shang, X. J. (2021). Analysis of semen quality of 38 905 infertile male patients during 2008-2016 in Wenzhou, China. *Asian J. Androl.* **23**, 1-5. doi:10.4103/aja.aja_83_20

Xu, H.-P., Yuan, L., Shan, J. and Feng, H. (2004). Localization and expression of TSP50 protein in human and rodent testes. *Urology* **64**, 826-832. doi:10.1016/j.urology.2004.05.012

Yoneda, R. and Kimura, A. P. (2013). A testis-specific serine protease, Prss41/Tessp-1, is necessary for the progression of meiosis during murine in vitro spermatogenesis. *Biochem. Biophys. Res. Commun.* **441**, 120-125. doi:10.1016/j.bbrc.2013.10.028

Yoneda, R., Takahashi, T., Matsui, H., Takano, N., Hasebe, Y., Ogiwara, K. and Kimura, A. P. (2013). Three testis-specific paralogous serine proteases play different roles in murine spermatogenesis and are involved in germ cell survival during meiosis. *Biol. Reprod.* **88**, 118. doi:10.1095/biolreprod.112.106328

Yuan, J., Wu, C. F., Huang, M. L., Zhou, J., Ben, W. and Zhang, G. M. (2015). TSP50 depends on its threonine protease activity and its interactions with TNF-α-induced NF-κB for its role in human cervical tumorigenesis. *Cell Biochem. Biophys.* **71**, 891-896. doi:10.1007/s12013-014-0279-8

Zhang, X. (2014). Depression of testes-specific protease 50 (TSP50) inhibits cell proliferation and induces apoptosis in laryngocarcinoma. *Tumour Biol.* **35**, 10781-10788. doi:10.1007/s13277-014-2090-y

Zheng, L., Xie, G., Duan, G., Yan, X. and Li, Q. (2011). High expression of testes-specific protease 50 is associated with poor prognosis in colorectal carcinoma. *PLoS One* **6**, e22203. doi:10.1371/journal.pone.0022203

Figure S1. Prss50-null mice were generated using CRISPR/CAS9 technology. A) *Prss50* mRNA sequence. Indicated in yellow is exon 2 (targeted exon). The 5' guide is indicated in purple and the 3' guide in aqua. **B)** Western blot of testis of WT and *Prss50*-null mice indicated the lack of PRSS50 in *Prss50*-null testis.

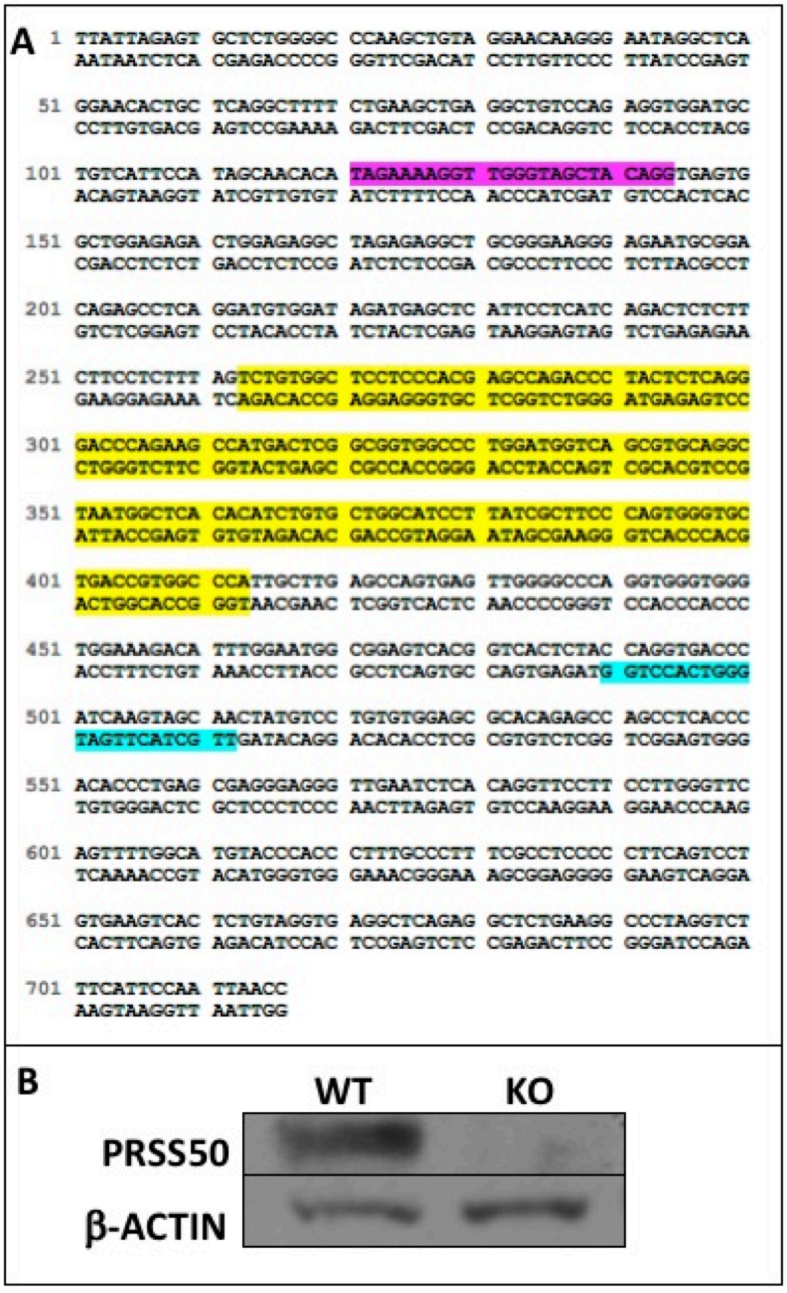

Figure S2. Staining of different markers of testicular cells and structures does not show differences between *Prss50*-null and WT mice. **A)** Testicular staining using the Leydig cell marker 3β-HSD. **B**) Testicular staining using the Sertoli and interstitial cell marker AR. **C**) Testicular staining using the spermatogonia cell marker PLZF. **D-E**) Testicular staining using the proliferation markers CCND1 and KI67. **F**) Testicular staining using the intracellular bridge marker TEX14.

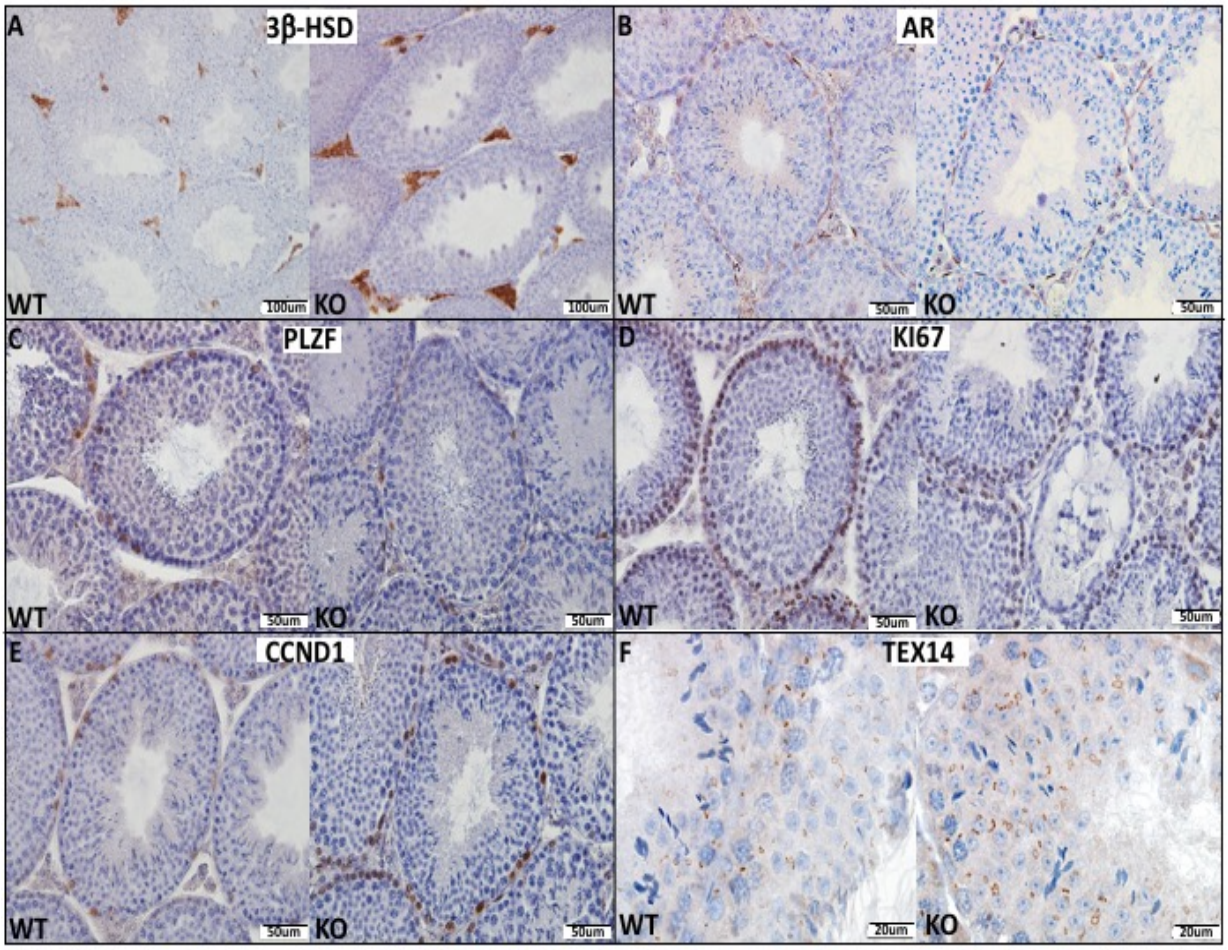

Figure S3. Level of Different testicular protein in *Prss50*-null mice. Comparison of the level of CCND1, FOX01, TEX14, and SOX9 between the testis of WT and *Prss50*-null mice. β-actin was used as an internal control. The ratio of Null vs. WT is indicated. None of the difference of ratios were statistically significant.

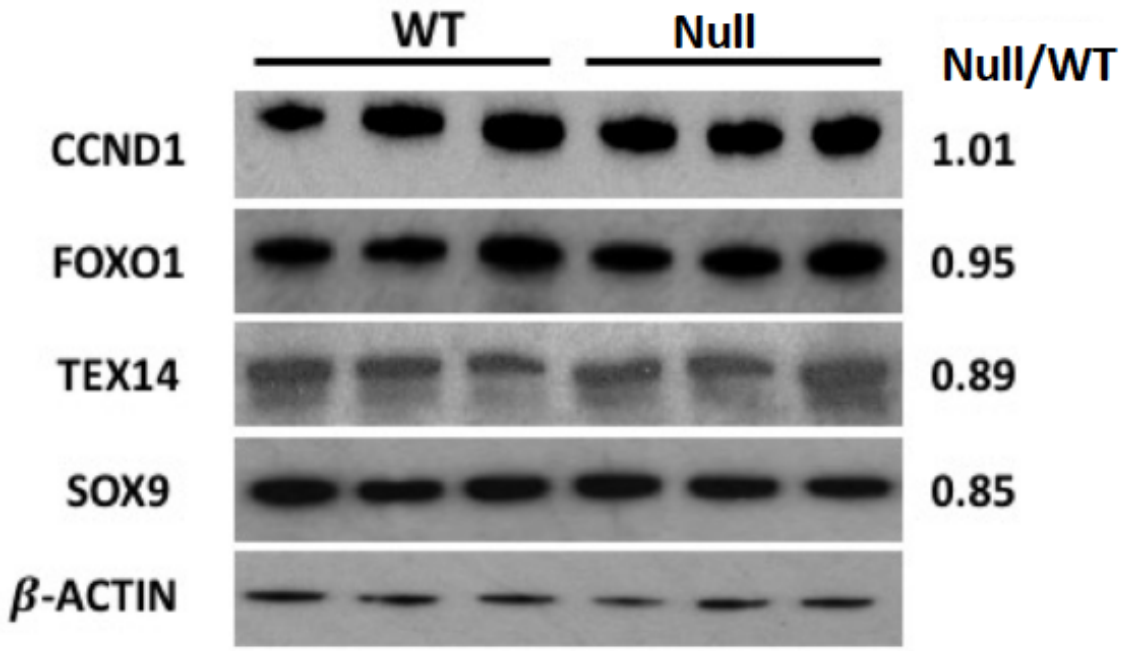

Figure 4S. Rules-based classification of sperm morphology. Sperm from WT and *Prss50*-null mice labeled with DAPI (head), MitoTracker (midpiece), and α-tubulin (tail) were subjected to HCA analysis. A total of 10,000 sperm from each sample were classified using a rules-based scheme shown. Numbers indicate the total number of sperm and percent of input.

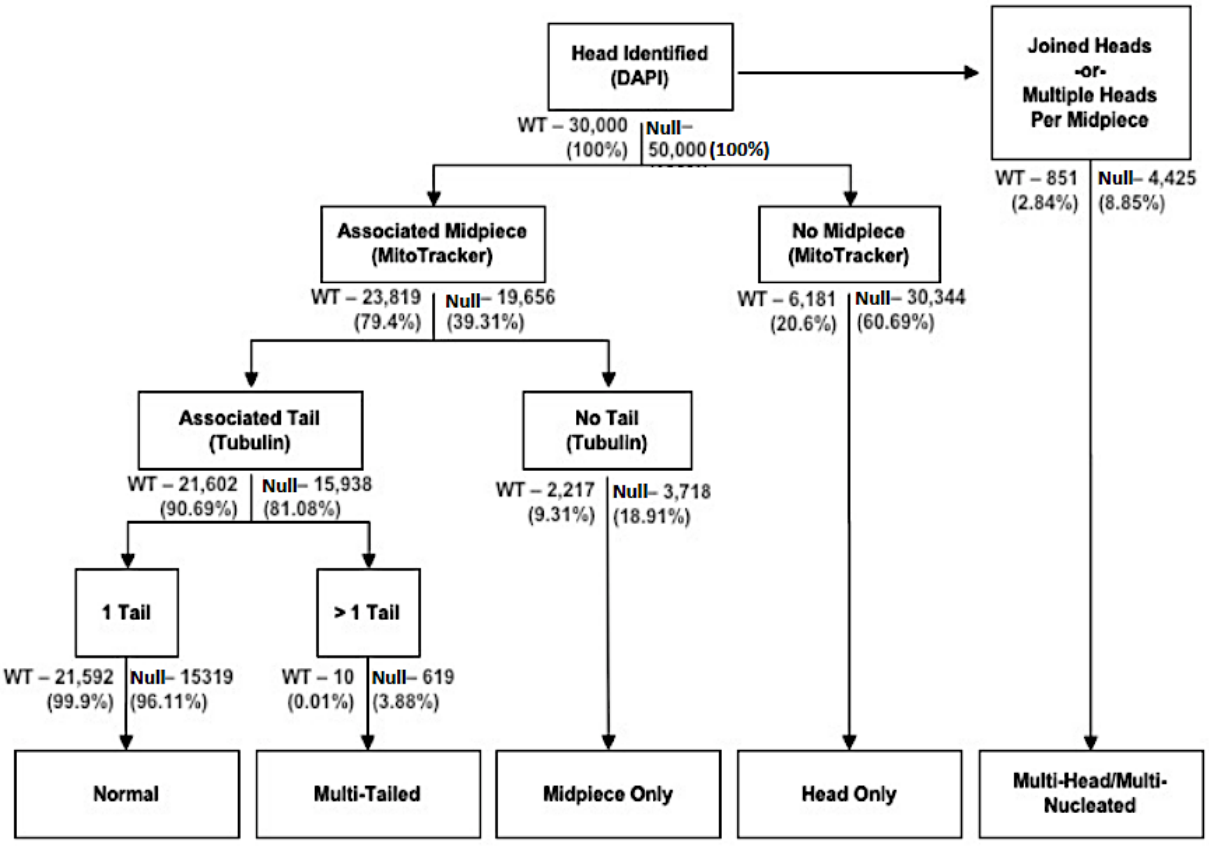

Figure S5. Sperm abnormalities in *Prss50*-null mice. *Prss50*-null sperm have multiple abnormalities including: conjoined (A-B), mitochondrial gaps in tail and bend tail (C-D), and multiple tail with single tails, or multiple heads and midpiece with a single principal piece (E-J).

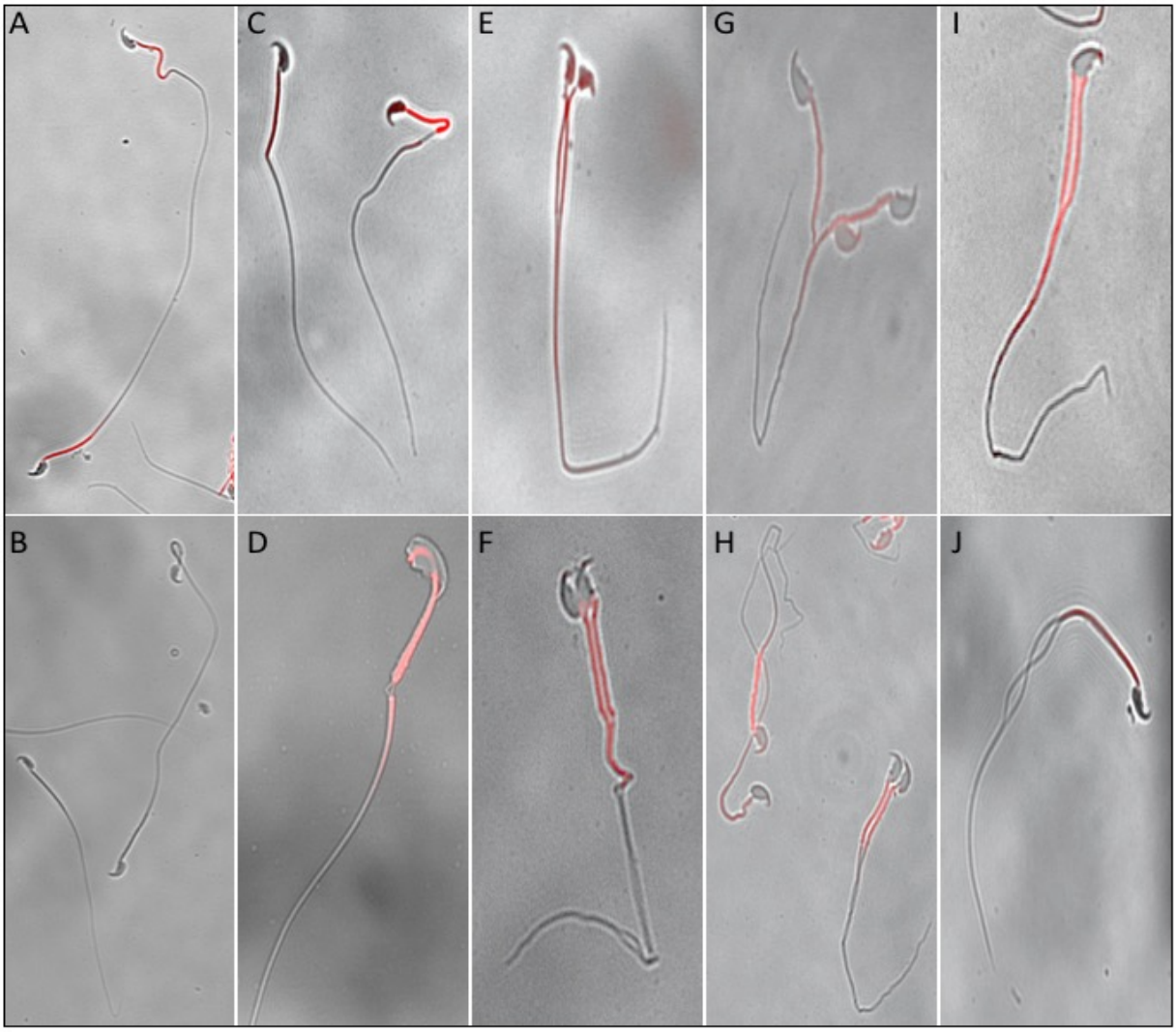

Figure S6. Sperm of *Prss50*-null mice do not have DNA damage based on Sperm chromatin structure assay (SCSA). Sperm heads from WT and *Prss50*-null mice labeled with acridine orange (AO). The SCSA simultaneously determines the % of sperm with high DNA stainability (%HDS) related to retained nuclear histones consistent with immature sperm; the % of DNA stainability versus red/red + green fluorescence (DFI); the count, area, circularity, and electricity. None significant difference between WT and null sperm was identified.

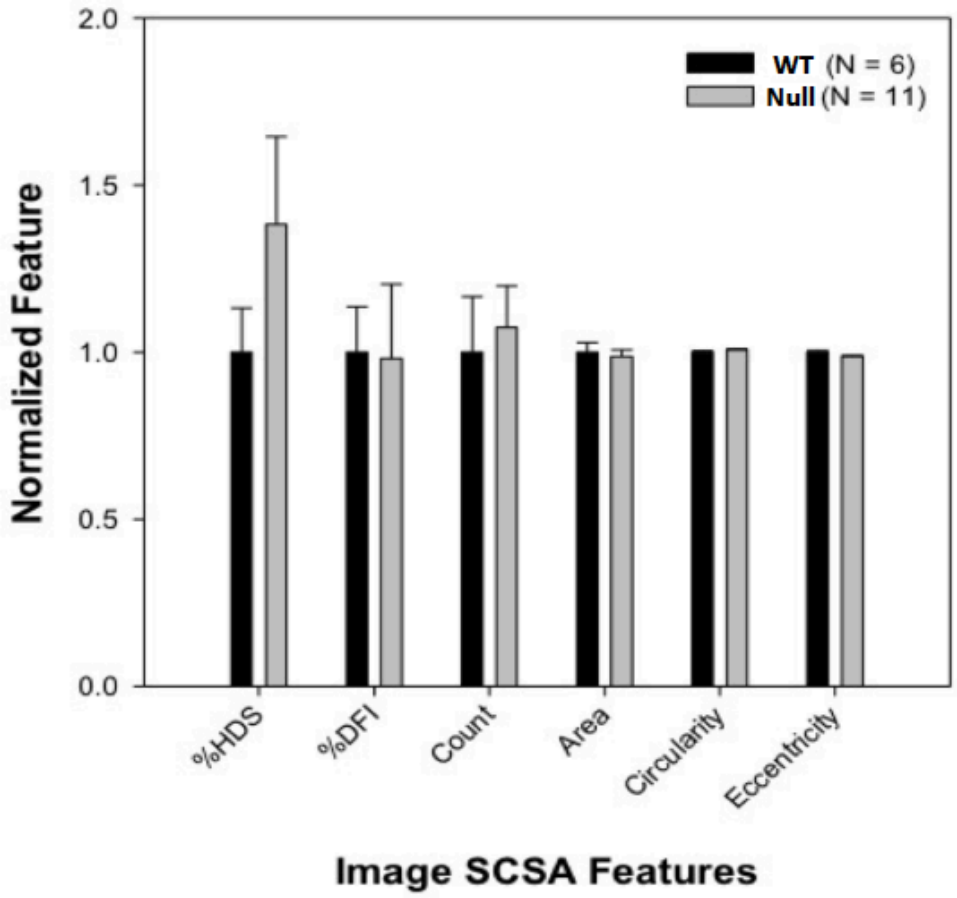

Figure S7. Testicular staining using AKAP4 does not show differences between *Prss50*-null and WT mice.

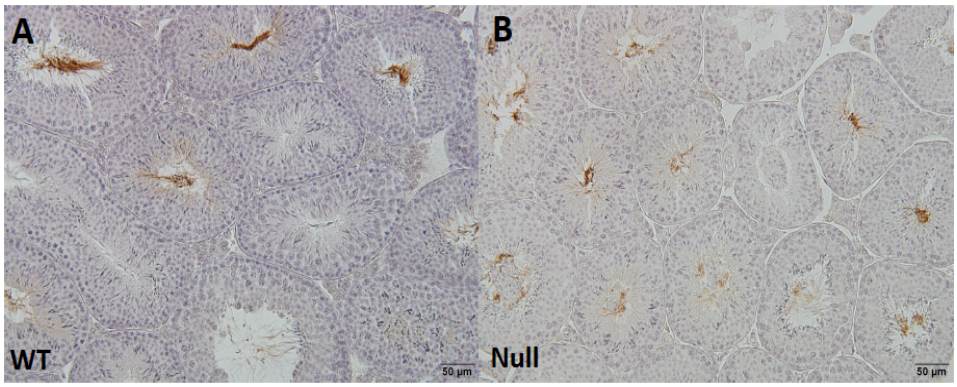

Movie 1. Frame from a microscopic video of WT sperm at 40X magnification (0.1x speed).

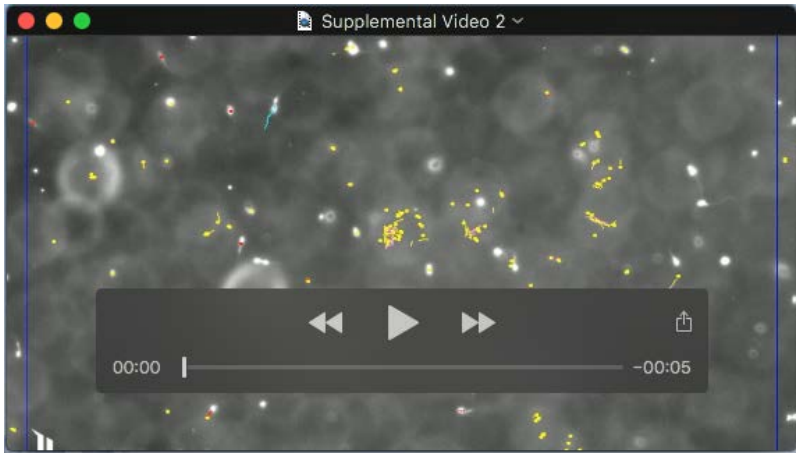

Movie 2. Frame from a microscopic video of *Prss50* null sperm at 40X magnification demonstrating a sperm with two heads (blue circle; 0.1x speed) as well as conjoined sperm.

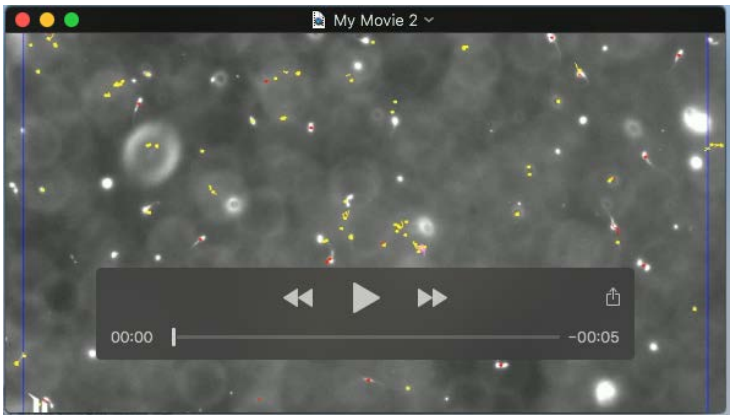

Movie 3. Frame from a microscopic video of *Prss50* null sperm at 40X magnification demonstrating conjoined sperm (blue circle; 0.1x speed).

Movie 4. Frame from a microscopic video of *Prss50* null conjoined sperm at 100X magnification (0.1x speed).

Movie 5. Frame from a microscopic video of *Prss50* null two-head sperm at 100X magnification (0.1x speed).